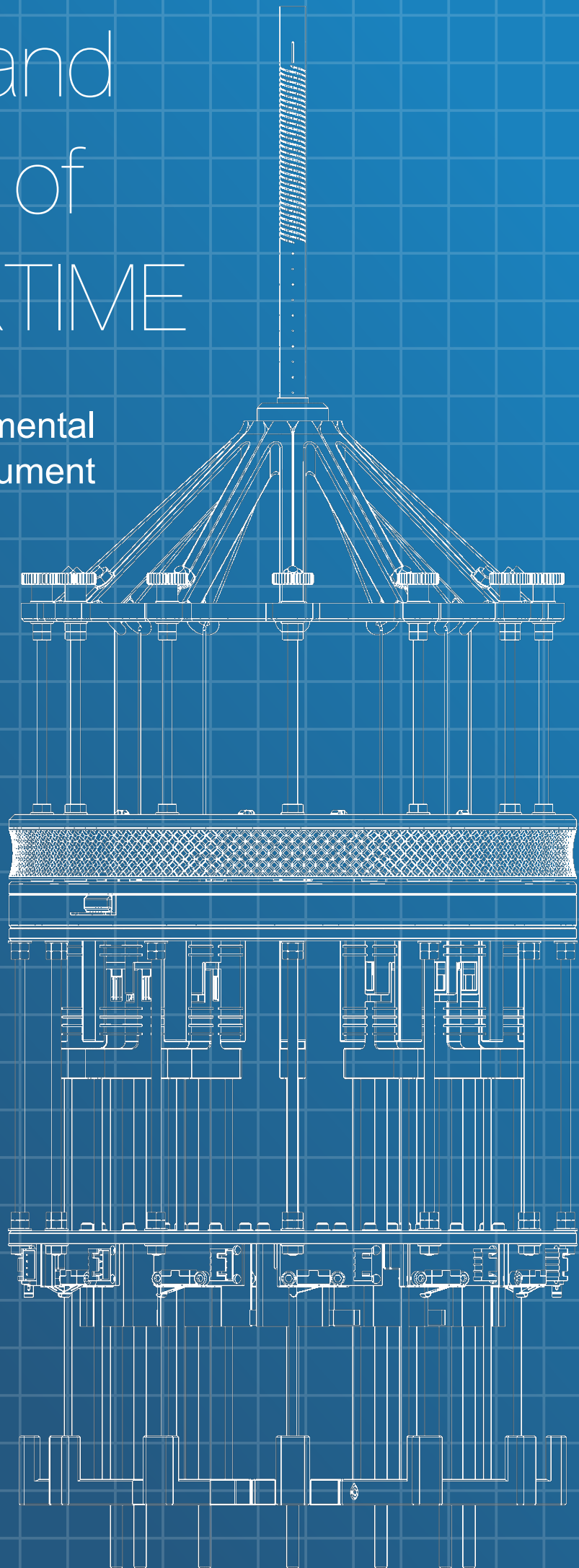


The Design and Development of Project OVERTIME

Open-source Versatile Experimental Robot for Tendon-driven Instrument Manipulation and Evaluation

Kees van den Berg



Design and Development of Project OVERTIME

Open-source Versatile Experimental Robot for
Tendon-driven Instrument
Manipulation and Evaluation

by

Kees van den Berg

to obtain the degree of Master of Science
at the Delft University of Technology,
to be defended publicly on Friday May 17, 2024 at 12:45 PM.

Student number: 4273281
Project duration: July 1, 2022 – 17 May, 2024
Thesis committee: Prof. dr. ir. P. Breedveld, TU Delft
Ir. F. Trauzettel, TU Delft, supervisor
Dr. Ir. T. Horeman, TU Delft

An electronic version of this thesis is available at <http://repository.tudelft.nl/>.

Preface

A long journey has come to an end. What started with knowing little to nothing about mechanical engineering a decade ago ended with a project building a prototype test setup for tendon-driven manipulators where special attention is given to the design of a low-cost custom build force sensor. The project started a while ago and definitely ended in OVERTIME. This thesis is part of my master's degree in Mechanical Engineering. The research is performed within the Bio-Inspired Technology (BITE) group at the Technical Univeristy Delft.

I want to thank my supervisor Fabian for the inspirational conversations and great discussions. You helped me continuing on with my journey and was always willing to help me out when necessary. Special thanks to Jacques from the meetshop for helping me out with the equipment for testing the prototype and Mauricio for helping me with testing the flexure design.

And thank my friends for the great dinners, breaks and laughs. You were always willing to give advice and ideas or provide a listening ear. The whole journey would not be possible to begin with if it wasn't for my parents, their unconditional support was the backbone that made graduating possible.

*Kees van den Berg
Delft, May 2024*

Contents

| | | |
|----------|---|-----------|
| 1 | Introduction | 3 |
| 1.1 | Minimally invasive surgery | 3 |
| 1.1.1 | Laparoscopy | 3 |
| 1.1.2 | Natural orifice transluminal endoscopic surgery | 4 |
| 1.1.3 | Steerable instruments | 4 |
| 1.1.4 | Tendon driven instruments test setups | 5 |
| 1.2 | Problem description | 5 |
| 1.3 | Goal of the thesis | 6 |
| 1.4 | Structure of the thesis | 6 |
| 2 | Design requirements | 7 |
| 2.1 | Functional requirements | 7 |
| 2.2 | Performance requirements. | 7 |
| 3 | Design | 10 |
| 3.1 | Concepts | 10 |
| 3.1.1 | Sub-functions | 10 |
| 3.1.2 | Actuation | 10 |
| 3.1.3 | Force sensing. | 10 |
| 3.1.4 | Coupling | 10 |
| 3.1.5 | Prototype concept | 11 |
| 3.2 | Design overview | 11 |
| 3.2.1 | Tendon diffuser | 13 |
| 3.2.2 | Motion Transfer Interface | 14 |
| 3.2.3 | MTI lock. | 14 |
| 3.2.4 | Assembly connector | 15 |
| 3.2.5 | Tendon tension sensor | 17 |
| 3.2.6 | Actuation unit | 21 |
| 3.2.7 | Structural cage elements. | 23 |
| 3.3 | Prototype | 24 |
| 3.3.1 | Prototype electronics | 24 |
| 3.3.2 | Prototype software | 24 |
| 3.3.3 | Final prototype | 25 |
| 4 | Prototype performance | 27 |
| 4.1 | Procedure. | 27 |
| 4.1.1 | Force sensor calibration procedure | 27 |
| 4.1.2 | Flexure displacement calibration procedure. | 27 |
| 4.1.3 | Flexure and Hall effect sensor hysteresis procedure | 27 |
| 4.1.4 | Hysteresis of prototype. | 27 |
| 4.1.5 | Manipulators test procedure | 28 |
| 4.2 | Materials and methods | 28 |
| 4.2.1 | Force calibration method. | 28 |
| 4.2.2 | Flexure displacement calibration method | 29 |
| 4.2.3 | Flexure and Hall effect sensor hysteresis method | 29 |
| 4.2.4 | Manipulators test method | 29 |
| 4.3 | Results | 29 |
| 4.3.1 | Force calibration results | 29 |
| 4.3.2 | Flexure displacement calibration results | 30 |
| 4.3.3 | Flexure hysteresis results | 31 |
| 4.3.4 | Hall sensor hysteresis results | 31 |

| | | |
|----------|--|-----------|
| 4.3.5 | Manipulators test results | 32 |
| 5 | Discussion | 34 |
| 5.1 | Prototype performance | 34 |
| 5.1.1 | Force calibration | 34 |
| 5.1.2 | Hysteresis | 34 |
| 5.1.3 | Hall effect sensor hysteresis | 35 |
| 5.1.4 | Hall effect sensor noise | 35 |
| 5.1.5 | System backlash | 35 |
| 5.1.6 | Manipulators test | 35 |
| 5.2 | Design evaluation & improvements | 36 |
| 5.2.1 | Manipulator adaptor | 36 |
| 5.2.2 | tendon diffuser | 36 |
| 5.2.3 | Motion transfer interface | 36 |
| 5.2.4 | MTI lock | 36 |
| 5.2.5 | Connector | 37 |
| 5.2.6 | Force sensor | 37 |
| 5.2.7 | Actuation unit | 37 |
| 5.2.8 | Changing manipulators | 38 |
| 5.2.9 | Electronics | 38 |
| 5.2.10 | Test setup software | 38 |
| 5.2.11 | Utility of the prototype | 38 |
| 5.3 | Requirements fulfillment | 39 |
| 5.4 | Further study & recommendations | 39 |
| 5.4.1 | Sensor leaf spring | 39 |
| 5.4.2 | Sensor interference | 39 |
| 5.4.3 | Interaction magnet and Hall sensor | 40 |
| 5.4.4 | Manipulator angle measurement | 40 |
| 6 | Conclusion | 41 |
| A | Bill of Materials | 46 |
| B | Test Setup Manual | 47 |
| B.1 | Assembly of the setup | 47 |
| B.2 | Using the setup | 48 |
| C | Additional Graphs | 49 |

List of Acronyms

| | |
|--------------|---|
| MIS | Minimally Invasive Surgery |
| NOTES | Natural Orifice Transluminal Endoscopic Surgery |
| DoF | Degree of Freedom |
| CAD | Computer Aided Design |
| FDM | Fused Deposition Modeling |
| MTI | Motion Transfer Interface |
| FEM | Finite Element Method |
| CNC | Computer Numerical Control |
| PLA | polylactic acid |
| SLA | Stereolithography |
| FBG | Fiber Bragg Grating |
| ADC | Analog to Digital Converter |

Abstract

Steerable medical instruments are used to reach difficult locations in the body during minimally invasive surgery (MIS). Researching these instruments helps to further improve their performance and reduce their size making them even less invasive. However, developing new technology can be expensive and often complete custom test rigs are build for these instruments. This thesis presents the design, manufacturing and validation of an affordable, open-source prototype test setup for multi-segmented tendon-driven manipulators aimed at stimulating academic innovation of these manipulators. The prototype allows manipulators to be changed swiftly for other or iterated designs. Computer aided design (CAD) was used to create the design and a novel low-cost 3D printed force sensor comprising a permanent magnet and Hall effect sensor was proposed costing only €2.11. The prototype uses readily available off-the-shelf components and custom 3D printed parts that can be manufactured using hobby grade fused deposition modeling (FDM) printers. Despite the prototype working as intended, there are some tolerance issues in the actuation mechanism and viscoelastic behaviour in the printed force sensor that requires more research. However, the prototype setup already has the potential to be used for preliminary testing of tendon-actuated manipulators. Future work should focus on improving the 3D printed force sensor for enhanced performance and reliability. This work contributes to the progression in testing and validating tendon-driven manipulators.

Introduction

1.1. Minimally invasive surgery

There are two main types of surgical procedures, open and minimally invasive surgery. Open surgery is characterized by making potentially large incisions in the body in order to gain direct access to the surgical site [1], and thereby giving the surgeon a direct view of their target. Conversely, in Minimally Invasive Surgery (MIS) procedures one or more small incisions are made in the skin or the walls of the hollow organs via the natural orifices of the human body to reach the surgical site [2]. To achieve this, MIS procedures generally make use of endoscopes to view the surgical site remotely.

Depending on the specific procedure, MIS generally has better outcomes than open surgery. MIS procedures do less damage to the patient, reduce blood loss, shorten hospital stays, and reduce analgesic use [3]. Lower mortality rates and a lower likelihood of re-admission and re-operation are also reported [4]. Elderly people in particular can greatly benefit from MIS as the number of complications and their severity are lowered, their hospital stays are shorter and less blood is lost compared to open surgery [5]. Cost savings of MIS over open or traditional surgery are also reported [6].

While MIS clearly has advantages over open surgery for the patient, they are more technically demanding for the surgeon and require specially adapted instruments. Slender tools are used in order to keep trauma to a minimum, typically 5, 8 mm or 12-20 mm instruments are used [7, 8].

1.1.1. Laparoscopy

With laparoscopy, the medical instruments are inserted through a trocar placed in the abdominal wall. Trocars provide an airtight seal between the outside world and the abdominal cavity [9]. This allows the abdominal cavity to be filled with CO_2 , which creates space in which to operate [10]. A schematic laparoscopic is shown in Fig. 1.1 by

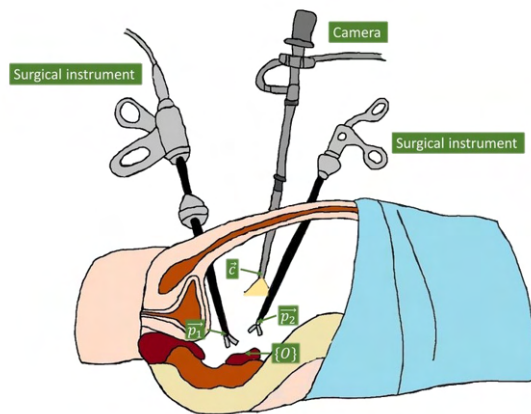


Figure 1.1: Schematic overview of a laparoscopic procedure by Rivas-Blanco et al. [11]. The figure shows the use of a camera and two surgical instruments to manipulate tissue inside the abdominal wall. Adapted from [11] under CC BY 4.0 license [12].

Rivas-Blanco et al [11]. However, the cavity is not always filled. Gasless laparoscopy can also be used, which can have further benefits in reducing pain and further shortening hospital stays, but is even more challenging for the surgeon to perform [13]. A distinction is made between single port and multi-port surgery. Multi-port surgery requires a number of incisions in different locations of the body, each port can admit one instrument to the body. Only one incision is made with single-port operation and special ports are used, some of which can house multiple instruments [14]. The instruments used in laparoscopy can be split in to two main types: rigid and steerable [9]. Rigid instruments can be either straight or pre-curved [15], and are mechanically less complex than steerable instruments, but are more difficult to operate with because of the fulcrum effect at the abdominal wall [9, 16]. Steerable instruments on the other hand give the surgeon more surgical freedom [9] by including some form of articulation. This typically takes the form of pitch and yaw joints at the distal

tip to mimic a wrist and thereby yielding two additional Degree of Freedom (DoF). Furthermore, articulated instruments make certain surgical tasks, such as suturing and knot-tying significantly easier. Steerable instruments are essential in single port laparoscopy where multiple instruments are inserted through one port [14, 16], as this clustering of instruments limits the manoeuvrability of rigid instruments in the body.

Laparoscopic surgery requires a camera and sometimes multiple instruments that all require precise choreography. A number of clinicians and assistants can be required to operate the laparoscope, manipulate surgical instruments or hold retractors. Fatigue of the person holding the laparoscope can lead to a reduction in quality of the view of the surgical site [17]. Furthermore, the fulcrum effect at the abdominal wall mirrors the motion of the surgeons or assistant's hand which can lead to confusion and additional fatigue [18]. Robot assisted surgery can help to circumvent these issues and can have better ergonomics and filter tremors from the surgeons' hands [19, 20]. A surgical robot is equipped with the tools and camera necessary to perform the surgery while the surgeon controls the robot remotely. The Da Vinci Surgical System is a well known surgical robot and their EndoWrist instruments has two DoFs in the wrist [21]. Steerable instruments with multiple DoFs are able to reach around obstacles, which can be useful to reach parts of the body that are otherwise difficult to get to [9, 22].

With older robotic surgery systems, the surgeon cannot directly sense the forces and pressure that is applied to the patient with a robotic system. This can lead to harmful situations for the patient, e.g. when too much force is applied to tissue [23]. Properly implemented haptic or other sensory feedback can prevent unnecessary harm and can also be used for tissue identification [23]. Haptic feedback could also help prevent the breaking of sutures when suturing [24]. However, the robotic system needs a way of determining the forces that are applied.

1.1.2. Natural orifice transluminal endoscopic surgery

Natural Orifice Transluminal Endoscopic Surgery (NOTES) is another form of MIS and uses the natural orifices of the human body to reach the surgical site without the necessity of an incision in the skin of the patient. Instead, an endoscope with special instruments is inserted in the body through one of the orifices of the body such as mouth, anus or vagina. Depending on the location of the surgical site tissue is manipulated in the lumen

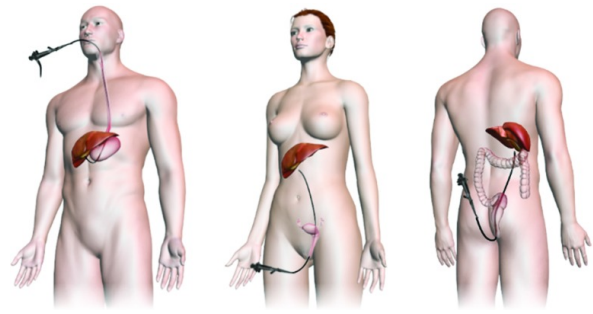


Figure 1.2: Three different NOTES approaches from left to right, trans-gastric, trans-vaginal and trans-rectal to reach the liver by Korzeniowski et al. [25]. Adapted from [25] under CC BY 4.0 license [12].

or an incision is made internally to further reach the target. Fig. 1.2, by Korzeniowski et al. [25], shows three different NOTES approaches to reach the liver. Modern MIS is moving more towards even less invasive surgery as the outcomes for the patient show very promising results [26]. However there are some limitations with these procedures. Flexible endoscopes are limited in their maneuverability due to limited steerable DoF, making surgery more difficult compared to alternative procedures [27]. Despite being a flexible instrument, only the tip of the endoscope is steerable. It is therefore necessary to develop multi-steerable instruments to overcome the issues with maneuverability and reachability.

1.1.3. Steerable instruments

Steerable instruments can be driven using, among others, electrical polymer, hydraulic, hygroscopic, magnetic, pneumatic, Shape Memory Alloy and tendon-driven actuators [28, 29]. Most commonly however, tendon or cable actuation is used for steering, which allows for the actuators to be located outside the body [30]. This can aid in the development of smaller instruments which in turn require smaller incisions, further reducing patient trauma. Tendon driven instruments also have a safety advantage over the alternatives. No high voltages, pressures or potentially toxic fluids are required for actuating the instrument inside the patient [21]. However, there are some points of improvement for tendon driven instruments such as hysteresis, friction, control and modelling [21]. In order to overcome these limitations and develop more reliable and precise instruments, further research is needed in this field. Examples of continuum tendon driven manipulators are shown in Fig. 1.3 [31].

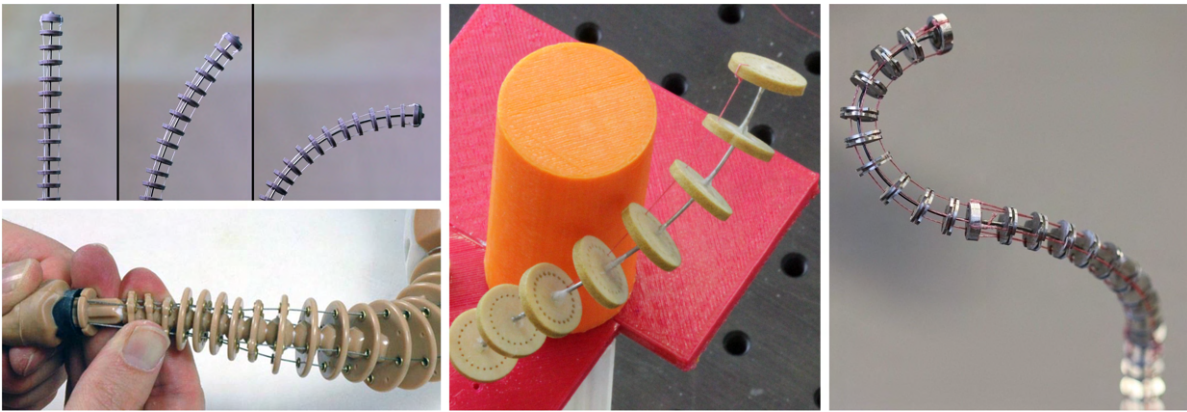


Figure 1.3: A few examples of continuum tendon driven manipulators. Adopted from the Continuum Robotics Laboratory [31]

1.1.4. Tendon driven instruments test setups

Researching tendon driven instruments requires experimental test setups to evaluate their performance. Different setup approaches can be found in literature. Luo et al [32] use a DC motor with ball screw guide to actuate the tendons and a webcam to track the motion of the instrument. The authors did not record the tension in the tendons. Lin et al [33] actuate their instrument directly with the tendons attached to servos without a reducing transmission and an optical tracking system is used for position tracking, the tendon tension is not measured. Wei et al [34] actuate the tendons using DC motors and a linear screw guide and a camera is used for position tracking. Tendon tension was recorded using JLBS-MD force sensors. Xu et al [35] directly connected the tendons directly to the motors via a spool without a reduction. A camera was used for motion tracking, no tendon tension was recorded. Qi et al [36] connected the tendons directly to stepper motors using a bobbin. A camera is used for motion tracking and tendon force was measured using a JLBS-MD-10 kg tension sensor. Eugster et al [37] connected the tendons to a linear screw guide driven by a DC motor. Six cameras were used for optical tracking of the instrument and the tendon tension was not measured.

Many publications do not include a way to measure tendon tension, even though this can be valuable data to assess the performance of the instrument and could help with the development of better control and prediction models for their actuation [38]. Most papers do not mention the shortcomings of the used setups and mainly discuss the performance of their proposed designs. However, friction in the test setup can negatively influence measurements [39, 40, 41]. Eugester et al [37] mention issues arising from nonuniform and

unrepeatable stresses due to manual tendon tensioning. Damage also occurred to the instrument during testing which was not resolved resulting in partially unusable data which could not be presented. It appears therefore that roboticists and control engineers in the field of tendon driven actuators could benefit from a test setup that includes a way of measuring tendon tension and allows for easy change of instruments. Researchers who specialise in medical robotics often do not have the mechanical design confidence to build customised test setups themselves. This discourages experimental work with an uncertain outcome, as the invested time and financial resources may not yield a satisfactory result.

1.2. Problem description

Developing new technology is expensive. It takes many resources such as work-hours, materials and equipment to create new innovations. Researchers can therefore be reluctant to test their device as one might break it, especially if only one prototype was built. Testing is necessary to determine the performance of a design. It is important to know the capabilities and limitations of an instrument in order to assess their possible use as surgical equipment. Generally speaking, the instrument is installed in a test setup with no ability to easily change the instrument without dismantling the setup. It can be time consuming to rebuild a setup for a new iteration or when the instrument breaks during testing.

As robotic surgery is being used for more interventions and moving more towards haptic feedback and collision detection it is important to quantitatively know the force characteristics of an instrument. However, many setups have no way of measuring force and mostly only focus on the kinematic properties of the instrument. This means

that there is no way of quantifying the force characteristics of the steerable instrument. Furthermore, interactions with the environment, e.g. manoeuvring through tissue, cannot be assessed force wise. Properly calibrated force sensors tend to be expensive, often costing multiple hundreds of euros each [42]. As tendon-driven steerable instruments often possess two tendons per Degree of Freedom (DOF), they would require correspondingly large numbers of sensors to track the tension on each tendon. A more affordable alternative could help in keeping the research expenses to a manageable level.

Researchers could also benefit from an open-source testing system. Anyone can improve the design for better compatibility and performance while being able to alter the design to their specific needs. This has the potential to evolve into a robust test platform for tendon driven instruments.

1.3. Goal of the thesis

The goal of this thesis is to stimulate the innovation of tendon-driven manipulators in academia by designing, building and validating an affordable, open source, force-sensing prototype test setup for multi-segmented tendon-driven manipulators, that allows for quick switching between different manipulator designs.

1.4. Structure of the thesis

This thesis continues with the design requirements for the prototype test setup in Chapter 2. Chapter 3 shows the design and build process from concepts via a computer model to the final physical design. The setup is tested in chapter 4 where special attention is given to the custom force sensor. Chapter 5 will discuss everything about tests, the limitations of the design, possible improvements and recommendations for future work. The project is concluded in chapter 6.

2

Design requirements

2.1. Functional requirements

In order to build a successful prototype a number of requirements were set of which an overview is given in Table 2.1. First of all, the prototype will be specifically designed for tendon-driven manipulators. The design focus will be primarily for continuum manipulators, but does not exclude discrete manipulators to be used with the setup. In order to be able to control the manipulator using a computer there must be some sort of electronically controllable actuator included in the prototype. An attachment is necessary between the actuator and tendon. Said attachment cannot be permanent to allow for interchanging the manipulator. Therefore the prototype must incorporate a way of connecting and disconnecting a distal section to a proximal section repeatedly. The distal section may only detach when the user intends to disconnect the distal section, it needs to remain assembled during use. This means that the proximal and distal sections must incorporate a fixation feature that can be actuated by the user. To gather data for evaluating the performance and behaviour of a manipulator, the prototype requires a features that can determine the tendon displacement and the tendon tension. The user must be able to calibrate these features. Manufacturing errors in the manipulator can introduce slack in the tendons which introduces backlash in the system. In order to remove this slack the prototype needs to be able to pre-tension the tendons before the test sequence starts. The file will be made open source to ensure free accessibility to a wide audience and allow for improvements to be passed on. Therefore, the setup must be designed with the consideration of readily accessible manufacturing techniques and incorporation of off-the-shelf parts. 3D printing such as Fused Deposition Modeling (FDM) is accessible to virtually everyone, especially in research institutes, and any custom part in the assembly should be designed to be easily manufactured using this process. For practical reasons as custom parts

will be 3D printed, it is required to model the parts using a Computer Aided Design (CAD) program. Therefore, in order to give people the ability to alter the design to their specific need, the setup must be built using a parametric CAD file. A number of different materials are available for FDM printing. However, some require experience or using the material or specialised printers. To make the design accessible for also non-experienced users, the printing material choice should be limited to polylactic acid (PLA).

2.2. Performance requirements

Depending on the research, steerable manipulator designs can have a single steerable segment or multiple segments. There are single segment designs that use only two actuators, one for each DoF. These designs often comprise a motor, e.g. a servo with a pulley wheel to which two antagonistic tendons are attached. However, it is not trivial to expand such an approach to multi-segment manipulators. Superposing the tendon displacement of the segments distal to the most proximal segment is necessary as the tendon displacement of more distal segments is influenced by the pose of the proximal segments. In order to accommodate for a variety in the amount of sections, the prototype needs to be designed for at least three sections. Most manipulators use four tendons to actuate one segment, therefore the design must be able to fit 12 actuators. However, to allow the design to serve as a flexible platform, the user may choose the number of to be installed actuators, depending on the number of steerable segments in the manipulator. For a minimum actuation range it is chosen to keep a 20 mm maximum diameter manipulator in mind, the segments of which may deflect up to 90°. This diameter is larger than the largest commonly used in a medical setting for endoscopes, to allow more diverse research to be carried out. The equation for the tendon actuation length can be derived from the sketch in Fig. 2.1

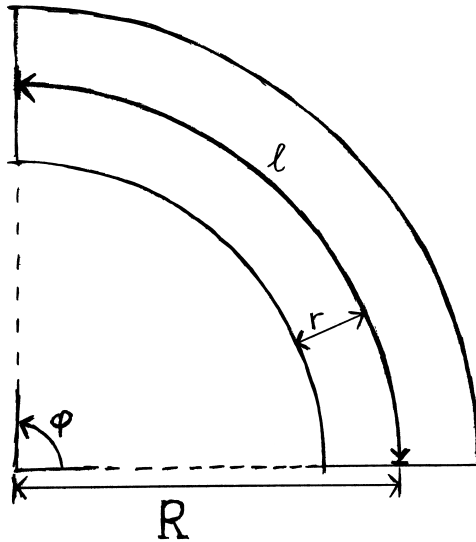


Figure 2.1: The amount of tendon displacement required to actuate a manipulator can be derived using the manipulator length l , radial tendon offset r and bending angle φ in radians. The curvature R results from the bending angle.

resulting in Eq. (2.1).

$$\Delta = r * \varphi \quad (2.1)$$

Where Δ represents the difference in tendon length between the neutral position and actuated position for a manipulator with tendons at a radial distance r from the neutral axis at bending angle φ . Note that this equation assumes the tendon to follow a smooth partial circular shape. When the tendon guide makes the tendon follow a discrete circular shape, the required actuation distance will be higher. Considering a theoretical maximum diameter of 20 mm, or 10 mm radial tendon offset, using a 20 mm diameter manipulator results in a minimum actuation range from the neutral position of 50 mm, or 100 mm between pulled and eased position. A manipulator with this diameter and three sections is curved by 270° at 50 mm tendon pull. The actuation resolution should be at least 0.5° for an instrument with 2 mm radial tendon offset. This converts to 0.017 mm resolution tendon actuation. To accommodate for the variety in manipulator diameters, the prototype must be able to receive manipulators up to 20 mm in diameter.

Manipulators that rely on a spring mechanism have the potential to be stiff and demand a large amount of actuation force, therefore 50 N is set as the maximum required actuation pulling force. In order to evaluate the performance of a tendon-driven manipulator the setup needs a way of determining tendon tension and tendon displacement. Industry standard force sensors are

expensive and the goal of the project is to create an affordable test setup. Therefore, the prototype needs a low cost $> \text{€}25$ method of measuring the tension per tendon. The user must be able to calibrate the tension sensor for accurate, $\pm 5\%$ full scale output, measurements.

The total cost of the setup should be $< \text{€}1600$. This is considering 12 tension sensors $\text{€}25$ each, 12 actuators $\text{€}75$ each, $\text{€}250$ for electronics and $\text{€}150$ for filament, fasteners and miscellaneous items. It is common for tendon-driven manipulators to incorporate one or more lumens through which smaller instruments, such as forceps and cutters, can be inserted. Therefore the prototype must have the option for accommodating these instruments. The user of the prototype will then be able to assess the performance of the manipulator with and without the instruments. The overall size of the prototype should be manageable and therefore stay within a $600\text{mm} \times 300\text{mm} \times 300\text{mm}$ space to allow for being carried by a person. To make the design as accessible as possible, the custom designed parts must be able to fit in a volume of hobby sized printers which are generally $220\text{mm} \times 220\text{mm} \times 250\text{mm}$.

Table 2.1: Overview of the requirements for the prototype test setup. The requirements are elaborated in the text.

| # | Functional requirement |
|-------------------------|---|
| 1 | The prototype must be designed for tendon driven manipulators |
| 2 | The prototype must use electronically controllable actuators |
| 3 | The prototype must include a non-permanent connection between the manipulator tendon and the actuator |
| 4 | The prototype must include a removable distal section |
| 5 | The distal section must be fixed to the proximal section during use |
| 6 | The prototype can determine tendon displacement |
| 7 | The prototype must include a feature to determine tendon tension |
| 8 | The tendon displacement measurement can be calibrated by the user |
| 9 | The tendon tension measurement can be calibrated by the user |
| 10 | The prototype can pretension the tendons |
| 11 | The design must be made open source |
| 12 | The design must be made using a CAD file |
| 13 | The prototype consists of off the shelf parts |
| 14 | 3D printing must be used to fabricate custom designed parts |
| 15 | The 3D printing material should be limited to PLA |
| Performance requirement | |
| 16 | The prototype must be designed for manipulators with least three segments, thus 12 actuators total |
| 17 | The total actuation range must be 100 mm |
| 18 | The prototype must be able to receive manipulators up to 20 mm in diameter |
| 19 | The prototype must actuate the tendons with a resolution of 0.017 mm |
| 20 | The prototype must be able to actuate up to 50 N pulling force per tendon |
| 21 | The tendon tension sensing must cost < €25 per tendon |
| 22 | The total cost of the setup must be < €1600 |
| 23 | The tendon tension sensing should be accurate within $\pm 5\%$ of full scale output |
| 24 | The prototype must include a feature a to accommodate insertable instruments in manipulators |
| 25 | The prototype must fit in a 600mm x 300mm x 300mm space |
| 26 | Custom designed parts must fit in a 220 mm x 220 mm x 250 mm 3D printer volume |

3

Design

3.1. Concepts

3.1.1. Sub-functions

From the requirements follow three main sub-functions: Actuation, force sensing and coupling. The actuation takes care of pulling and easing the tendons of the manipulator. Force sensing measures the tension in the tendons which is to be logged on a computer. The coupling subsystem enables coupling and decoupling of the manipulator to the test setup.

3.1.2. Actuation

The requirements state that the setup is to be electronically controlled via a computer. There are basically five types of actuation possible: Electromagnetic, hydraulic, pneumatic, piezoelectric and shape memory alloy. Considering the range of motion requirement and the requirement to use off the shelf and affordable materials eliminates piezoelectric and shape memory alloys for actuation. Hydraulic and pneumatic actuation generally require special and expensive hardware for precise control. Though hydrolic and pneumatic actuators have the potential to be used in MRI environments. Therefore, electromagnetic actuation is chosen to drive the setup as these actuators are abundantly available for relatively low prices and they can be controlled using simple electronics.

3.1.3. Force sensing

A number of different options exist for measuring force. Strain gauges placed in a Wheatstone bridge are typically used in application where high accuracy and precision is desired. However, these sensors are fairly costly. Fiber Bragg Grating (FBG) also offers high precision and works with optic fibers with special filters that change the color spectrum of the light as the fibers deform. Special and expensive equipment is needed to use this method of measuring. Force sensitive resistors directly relate force to an electrical output. The

resistance of these sensors change with change in load. They have a lower accuracy than strain gauges, but are lower priced. Force can also be measured mechanically using linear springs. This principle can be commonly found in analog weighing scales and spring scales. The extension of the spring moves a indicator over a dial so the force can be read by the user. This principle can be converted to an electronic sensor when the distance is measured electronically. This method will be further explored.

3.1.4. Coupling

The coupling subsystem needs to fulfill the requirements regarding attaching a manipulator to the test setup. This coupling must be non-permanent to allow instruments to be interchanged as stated in the requirements. Both a motion coupling unit as a structural connection unit are required.

The tendons of the manipulator must be pulled and eased which can be achieved both by rotation and translation. This does not dictate the actuation used as the motion can be converted before and after the coupling interface. There are four types of motion transfer possible as indicated in Fig. 3.1. That is transferring motion at the coupling interface from the proximal to the distal section. The distal section is defined as the removable part of the setup into which a manipulator can be installed. The two most straightforward are rotation to rotation and translation to translation. However, also rotation to translation and translation to rotation is possible. A motion transfer interface can be designed based on the chosen method.

The structural coupling is mainly depending on the desired engagement of the distal & proximal section, that is how the two section are approached, and the shape of the system, round, square, etc. Four types of engagement can be distinguished as shown in Fig. 3.2. The four engagement types are axial-axial, axial-lateral, lateral-

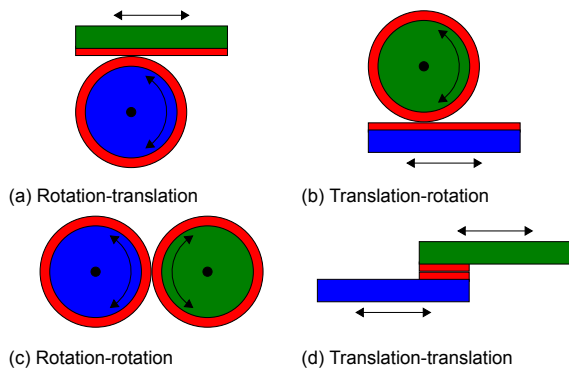


Figure 3.1: The four different ways of transferring motion. The distal section is colored green and the proximal section is colored blue. The red parts on the proximal & distal sections resembles the Motion Transfer Interfaces (MTIs). The arrows indicate the possible directions of motion.

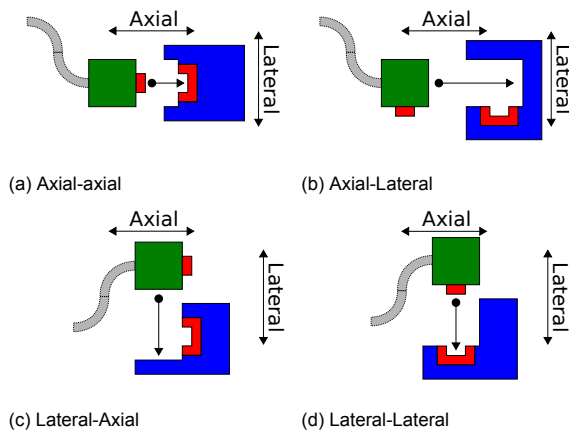


Figure 3.2: The four different ways of engaging. The distal section is colored green and the proximal section is colored blue. The gray curved piece resembles a manipulator. The red parts on the proximal & distal sections resembles the Motion Transfer Interfaces (MTIs). The arrow with one dot is indicative for the direction of engaging the distal section to the proximal section. Which is either in axial or lateral direction which are indicated with pointy arrows.

axial and lateral-lateral. The engaging is two parted, the first part indicates the direction how the distal section is moved to the proximal section, the second part indicates how the motion transfer interfaces are oriented, both from the perspective of the distal section. Axial means along the longitudinal axis and lateral is perpendicular to that axis. Inspiration for the coupling interfaces was drawn from [43] where patents for medical coupling interfaces were investigated.

3.1.5. Prototype concept

An overview diagram of the prototype concept is shown in Fig. 3.3. The different colors indicate the different sub-functions and subsystems of the prototype. From left to right: The manipulator and

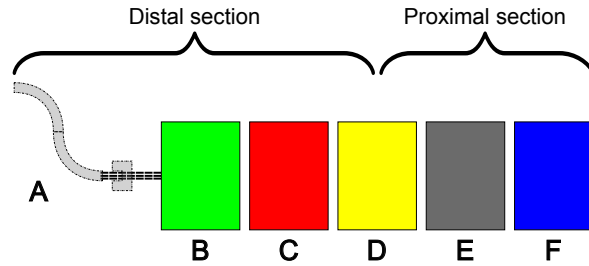


Figure 3.3: Block overview of the concept. The colors represent different subsystems: A = manipulator and adaptor, B = tendon diffuser, C = motion transfer interface coupler and lock, D = structural coupler, E = force sensing, F = actuation. The system is split in a proximal and distal section at the structural coupler.

adaptor, tendon diffuser, motion transfer interface coupler and lock, structural coupler, force sensing and actuation. The manipulator will be provided by the user of the prototype. It needs to be coupled to the system using some sort of an adaptor which can be customized to fit the manipulator in question. The tendon diffuser will guide and divert the tendons from the relatively small manipulator to the potentially larger grid of actuators. This is followed by a coupler for the motion transfer interfaces. The concept is split in a proximal and a distal section that is split at the structural interface. Force sensing takes place in the proximal section and will be connected to the actuators.

3.2. Design overview

To facilitate convenient testing of multiple tendon-driven manipulator designs or to easily repair broken manipulators, the prototype design was split into a proximal and distal section at the yellow coupling in Fig. 3.4. Electronics, actuation and tension sensing are located in the proximal section, while the manipulator can be attached to the distal section. In this way, the manipulator being tested can first be assembled on to the distal section and its tendons managed more easily. Once the manipulator and its tendons are in place, the distal and proximal sections are mated and locked together, connecting the tendons of the manipulator to the actuation and sensing package in the proximal section. All the electronic parts are deliberately placed in the proximal side to prevent electronic connectors to be a necessity in the coupler.

A sectioned overview of the final design is shown in Fig. 3.4. The tendon diffuser (Fig. 3.4, green) is the most distal part of the distal section. It is roughly cone-shaped and is responsible for two main functions. Firstly, it features a locking section at its pointed end to which the manipulators can be firmly but removably attached. For this pur-

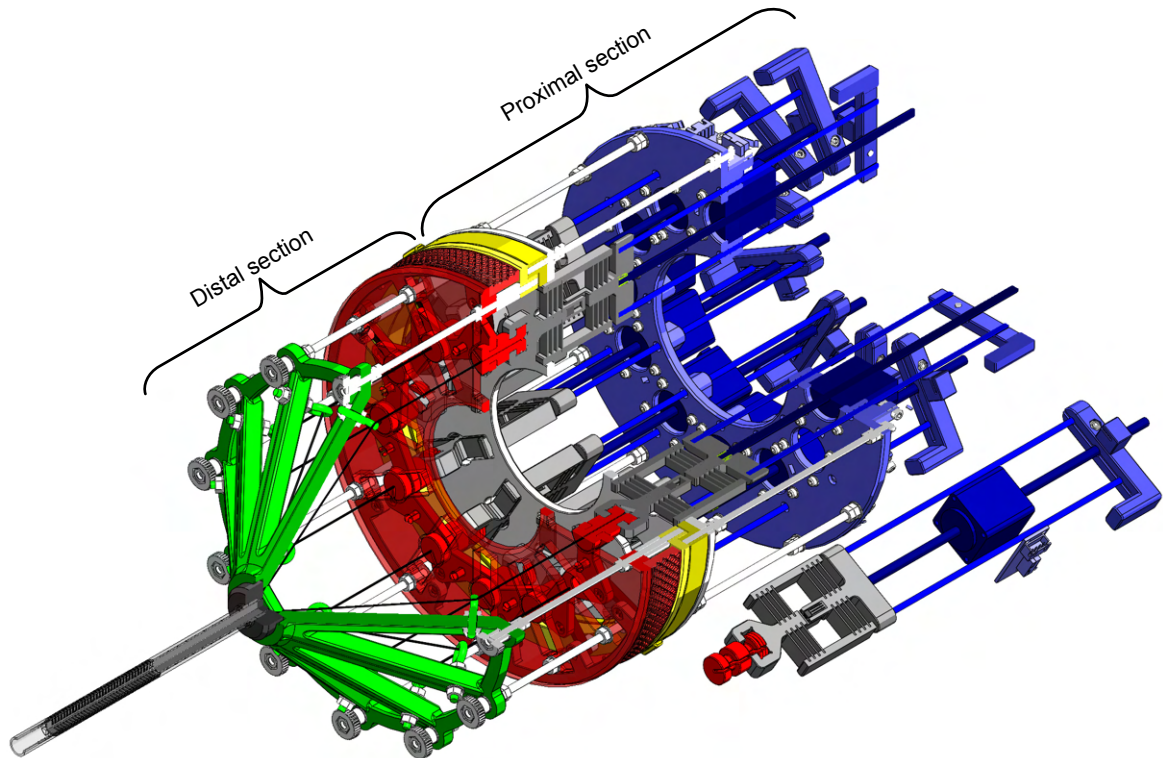


Figure 3.4: A sectioned view of the CAD model of the prototype design where one quarter of the design is cut away to reveal the internals. One actuation section is exploded (lower right) and shown next to the assembly. A dummy manipulator is attached to the setup for visual purposes. Each color in the overview represents a sub function of the system, from left to right: Tendon guidance (green), Motion Transfer Interface (MTI) locking (red), coupling (yellow), tendon force sensing (grey), tendon actuation (blue) and structural cage elements (white). Different shades of color are used to distinguish between multiple parts in a sub system.

pose, it features a simple bayonet-style fitting that can accept manipulators up to an outer diameter of 20 mm. Secondly, the diffuser guides the tendons exiting the manipulator outward in a radial direction to make room for the actuation units. This is achieved via a set of eye bolts attached to the diffuser's inner surface. The eye bolts redirect each tendon to run co-axially with its actuator, which helps to remove any unwanted moments from the actuation system.

Connected proximally to the diffuser via a group of threaded rods is the Motion Transfer Interface (MTI) system (Fig. 3.4, red). The tendons of the manipulator are fixed to the distal MTI, which is a cylindrical part with circumferential grooves. The MTI system allows the tendons to connect removably with the actuation and sensing assemblies using shape locking. When the distal section is attached to the proximal section, the distal MTI engages with the proximal MTI. The proximal MTI has a fork like feature that receives the distal MTI when the distal section is connected. A locking mechanism allows the distal MTI to stay in place when the distal section is not attached to the prox-

imal section.

Next to the MTI system is the coupling interface (Fig. 3.4, yellow) which is also connected to the group of threaded rods of the MTI system. It consists of two rings with locking features, one ring on the proximal section and the other on the distal section. The ring of the distal section is connected to the same group of threaded rods as the MTI system, whereas the ring of the proximal section is connected to another group of threaded rods. This coupling interface is responsible for a structural connection between the distal and proximal section. The proximal section receives the distal section axially, which when seated properly can be rotated clockwise to be locked in place.

When the distal and proximal sections are connected, the distal MTI is held by the tendon force sensor (Fig. 3.4, gray). It consists of a holder for the distal MTI, leaf springs, a magnet, a Hall effect sensor and a feature allowing to be fixed to the actuation unit. This sensor measures the tension in the tendons of a manipulator using the Hall effect sensor and leaf springs. The springs extend under load and the Hall effect sensor measures the

extension. Using a microcontroller, the raw Hall sensor values are converted to newtons.

Directly connected to the force sensor is the actuation unit (Fig. 3.4, blue). This unit comprises a non-captive stepper motor, linear guide, limit switch, end bar and base plate. The motor is bolted to the base plate, the linear guide slides through the base plate which also acts as a bushing, the limit switch and end bar are used for calibrating the actuation unit. Actuation is done by pulling and releasing the tendons. The non-captive stepper motor in cooperation with the linear guide converts rotational motion to a translation.

The threaded rods mentioned before form a structural cage (Fig. 3.4, white). A solid structure is realised together with the plates, coupling rings and diffuser cone. Nuts are used to fix all the parts in place.

The brain of the setup is an Arduino microcontroller. Allegro A4988 stepper drivers are used to control the stepper motors. All the drivers, Hall effect sensors and limit switches are connected to the Arduino using a breadboard and electrical wires. A 24 V power supply powers the system.

Arduino firmware controls the microcontroller. The Arduino platform is open-source and practical for prototyping. The software controls the motors, reads sensor data and sends data to the computer to be stored. A Matlab script on the computer gathers the data to enable manipulation and plotting to give insight in the performance and behaviour of the tested manipulator. The data can be used to publish the results and improve the manipulator.

FDM 3D printing has a very low barrier to entry, as modern hobby grade machines can be purchased for as low as €200 [44] and the required printing materials both cheap and commonly available. FDM machines also have a very low skill and experience requirement for operation. Finally, the design files required for printing are standardised and can easily be distributed online for convenient access. All custom parts in the assembly are designed from their initial concepts with FDM printing in mind, even before proceeding to their initial versions in CAD. Where necessary, design features were added to enhance the overall quality of the 3D printed part. These features are detailed wherever their respective host parts are discussed.

3.2.1. Tendon diffuser

The most distal part of the distal section is the tendon diffuser. Here a manipulator can be placed in an adaptor which can be fitted into the circular coupler. The adaptor can be customized to receive any manipulator without the need to build a

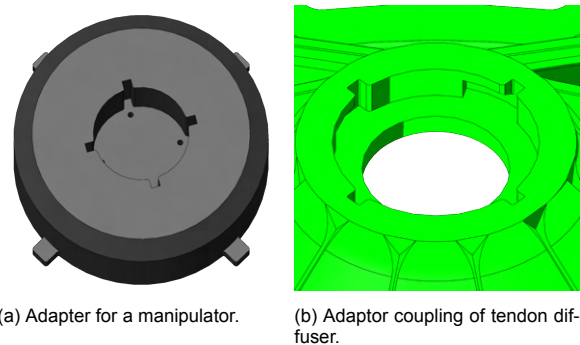


Figure 3.5: Example of an adapter for a manipulator and closeup of the adapter coupling of the tendon diffuser. The adaptor can be placed in the coupler of the tendon diffuser. The tabs on the adaptor fit in the cutouts and grooves of the tendon diffuser.

new tendon diffuser. The adapter has protruding tabs that fit into cutouts in the diffuser and can be twisted into place as the tabs follow the grooves in the diffuser as shown in Fig. 3.5. The parts are held together with a friction fit.

The chosen implementation for actuating the manipulator is not compatible with a number of tendons bundled together in a small circular pattern on the manipulator. Therefore, the tendon diffuser diverts the tendons from the small manipulator diameter to the larger actuation diameter. Stainless steel eye bolts are placed inside the cone and fixed to the spokes with nuts. The eye bolts are used to route the tendons co-linear with the direction of actuation. This ensures proper loading of the tendon force sensor and prevent sideways or moment loads to the actuator.

The diffuser cone is made up of spokes to reduce material use compared to a solid cone shell. This also allows the user to manage the tendons more easily when installing a manipulator. The inner wall of the spokes form overhangs. An overhang is any part of a model that extends horizontally without any support beneath it. A vertical wall is defined as 0° overhang whereas a horizontal bridge has a 90° overhang. Printing overhangs can be challenging as a steeper overhang is more prone to failure due to principle that FDM is based on, namely adding layers of material on top of each other. Often 45° is used as default threshold value in slicing software for overhang angles to start using supports. These supports are added to the model in the slicer to form a foundation for the overhangs to rest on. However, supports reduce print quality, increase risk of print failure and, depending on the model that is printed, can significantly increase print time and material usage. Therefore it is preferred to avoid the need for supports in a model. The spokes are angled at 47.5°

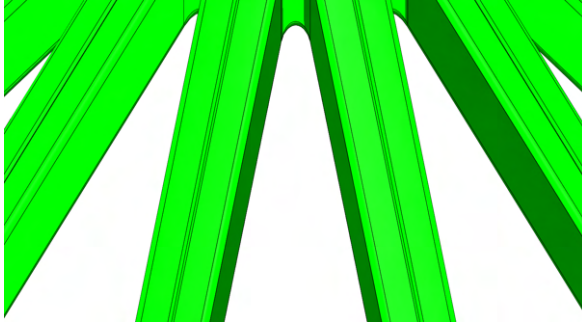


Figure 3.6: Close up of the grooves in the tendon diffuser. The grooves are added to improve print quality.

°overhang and printed without supports. This angle is a balance between not requiring supports, quality and print time as a more shallow overhang means a higher part which requires more material and time to print.

Every spoke has a vertical seam when sliced for printing. Ideally this seam is not placed at the overhang as there is minimal material beneath to support the start of an extrusion. In order to control the location of the seam for each spoke, a small groove on the outside of the spokes was introduced as shown in Fig. 3.6. As the groove has the sharpest corner in the cross-section of each spoke, the slicer's default setting will put the seam in the groove instead of any of the other corner on the spokes. In this way, the seam of each wall is not at the overhang but on top of already printed material, which improves the quality of the part.

The spokes are attached to a structural ring at the base of the tendon diffuser to which twelve ears are attached. The ears have mounting holes for assembling the structural threaded rods. The spokes are aligned with the threaded rods to prevent bending loads to the ring and direct the loads to the structural cage. The spokes are slightly offset inwards to the ring to allow for proper assembling of the diffuser to the rest of the distal section.

3.2.2. Motion Transfer Interface

The tendons routed through the diffuser need to be attached to the actuator. The motion transfer interface (MTI) was introduced that allows for a non permanent connection between the tendons of the manipulator and the actuation unit. This interface consists of two parts, one in the distal section and the other located proximally shown in Fig. 3.7c.

The distal MTI is a cylinder with two large circular grooves, a slit along the length of the part, one small circular groove and a dimple in one face as shown in Fig. 3.7b One of the large grooves is engaged by the proximal MTI, the other groove is used to lock the distal MTI in place when the distal

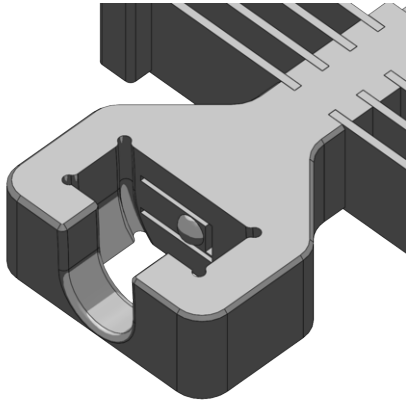
section is placed and removed from the proximal section, this is further explained in Section 3.2.3. The slit allows for easy threading of the tendon into the distal MTI. To fixate the tendon, it can be wound around the cylindrical section in a small groove. Using a knot and a drop of cyanoacrylate glue prevents the tendon from loosening. The dimple in the face of the part receives a similar shaped dome from the proximal MTI that locks the parts together when the distal section is attached to the proximal section.

The proximal MTI is integral to the tendon tension sensor (Section 3.2.5) and features a fork like structure, shown in Fig. 3.7a to engage with and hold the distal MTI when the distal section is connected to the proximal section. It consists of a U-shaped fork that receives the first large groove of the distal MTI. A spring loaded dome on the proximal MTI fits into a matching concavity on the head of the distal MTI. This keeps the parts connected and prevents the distal MTI from separating when the two sections are coupled. The spring is a cantilevered leaf-spring type and is also integral with the force sensor flexure. As the distal section is fixed into place by twisting it, the MTIs engage and lock together. Because engaging the two section is done using a twisting motion, the U-shaped slot in the proximal MTI is slightly curved to match the curvature of the path the distal MTI takes when being connected.

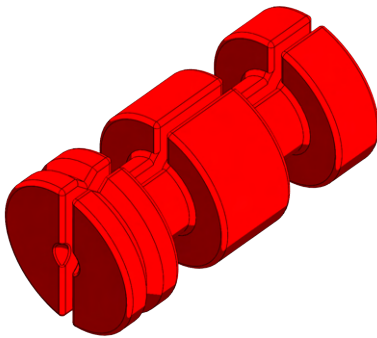
3D printing is also used for the MTI parts. Therefore attention was given to some details of the models. FDM was used to create the proximal MTI. The cantilevered leaf spring of the proximal MTI was extended on the bottom of the leaf to form a bridge instead of a pure cantilever as can be seen in Fig. 3.7a. This extension needs to be cut away after printing for the spring to move properly. Its function is to eliminate the need of support material under the cantilever during printing. Bridging, i.e. printing over a gap or hole without supports, generally gives a cleaner and better result than using supports. The distal MTI was printed using Stereolithography (SLA). FDM did not give satisfactory results for this part. The cylindrical shape in combination with overhangs caused by the grooves made achieving clean and useable results using FDM challenging.

3.2.3. MTI lock

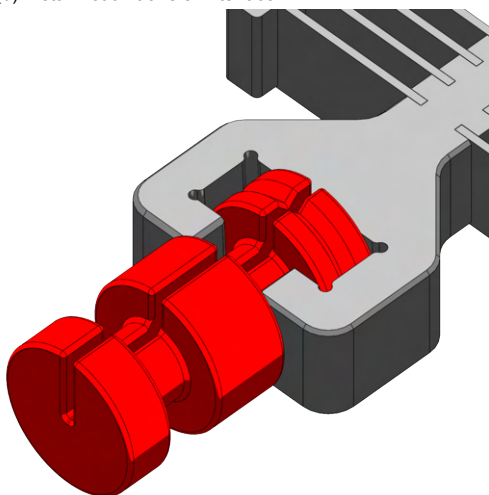
All the MTIs need to be in the same plane when the distal section is connected or disconnected. This is to ensure the distal MTIs are in the right spot when they engage with the proximal MTIs. The function of the MTI lock is to hold the distal MTI in position when the distal section is discon-



(a) Proximal motion transfer interface



(b) Distal motion transfer interface



(c) motion transfer interfaces connected

Figure 3.7: The proximal and distal motion transfer interface parts. The proximal MTI receives the distal MTI when the distal section is connected to the proximal section. The dotted lines show the hidden contours of the parts not visible from the current perspective.

connected from the proximal section. Once the connection is made, the lock can be released after which the actuators can move the attached manipulator. Locking the MTIs is realised using form closure or shape locking. The distal MTI has a circumferential groove into which locking tabs located in the distal section can be swiveled to hold the distal MTI in place. The locking tabs can be manually actuated by turning the locking collar. A four bar linkage, consisting of the blue disk, orange ring, yellow locking tabs and grey links (Fig. 3.8), moves the locking tabs into the locked and unlocked position. There are 12 locking tabs working in unison to lock all the distal MTIs when the orange ring is rotated. One locking tab locks one half of the MTI while another locks the other half as shown in Fig. 3.8. The locking tabs are placed at the proximal side of the distal section. This was done to ensure that the tabs would be pressed against the blue plate in Fig. 3.8 instead of being pulled away and potentially become loose when the user would connect and tighten the tendons to the distal MTI.

The red pins connecting the blue plate and yellow locking tabs use the snap-fit principle to hold the parts together. This allows for convenient installation of the parts without extra hardware such as nuts and bolts being a necessity. The grey link also connects the yellow part and orange ring using the same snap-fit principle. Fig. 3.8 shows small features extending from the orange ring's inner surface. These features are cantilevered to create a spring and hold the ring in place when rotated into locked or unlocked positions. This is done to prevent any unwanted actuation of the ring. The small features get 'stuck' behind the protrusions on the blue disk. By simply overcoming the force needed to move the spring loaded features one can rotate the ring by hand. Furthermore the bottom parts of these cantilevers are extended to meet with the ring as was done with the proximal MTI (Section 3.2.2) which improves print quality. These extensions also need to be removed after printing. Custom supports are created for snap-fit pins on the grey links as the slicer did not generate good quality supports. All the parts of the MTI lock were printed using FDM.

3.2.4. Assembly connector

To couple the distal section to the proximal section a connector is needed. The connection needs to be rigid to ensure the design forms one complete unit and stays connected during use. When the manipulator is actuated, the force sensor needs to be able to move through the connector interface when the manipulator is being actuated. The cou-

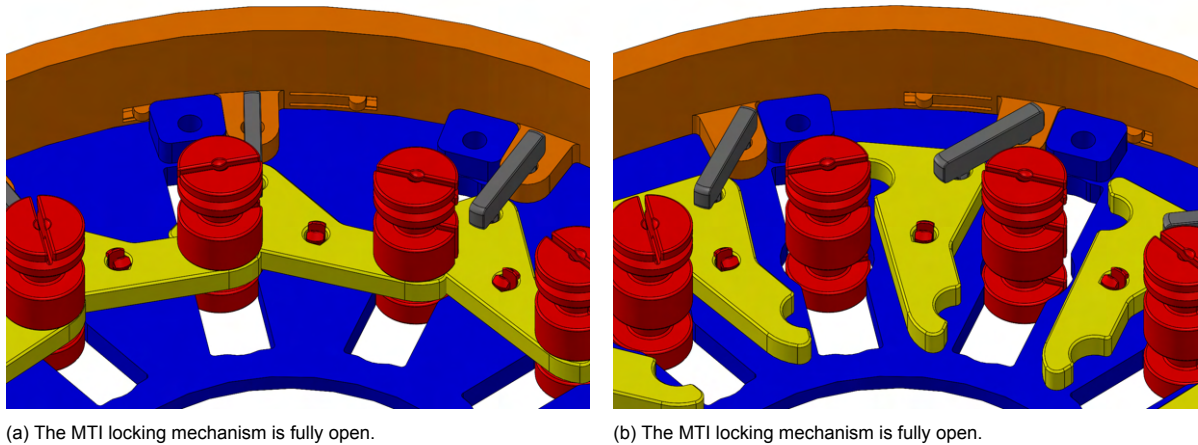


Figure 3.8: The MTI lock can be opened and closed by rotating the orange actuation ring. The yellow tabs engage with the grooves in the red distal MTI. When the lock is fully opened, the actuators can move through the cutouts in the blue plate. The grey links transfer the motion of the orange ring to the yellow tabs which swivel around the red pins.

pler is designed with the actuation units in mind. These will be placed in a pattern as will be discussed in Section 3.2.6. This pattern is circular. Therefore, the connector consists of two rings at the circumference of the system, one proximal and one distal, so that there is no interference with the actuation mechanism which is kept inside these rings. The connection is made as follows: The distal side is moved axially to the proximal side. Radially patterned tabs and the cantilevered locking tabs on the distal side (Fig. 3.9) fit into the respective cutouts of the proximal side. When properly seated, the distal side can be rotated clockwise until the locking tabs of the distal side engage with the locking tab cutouts of the proximal section. These tabs slide in the grooves of the proximal side when the distal section is rotated. The rings mate concentrically and restrict radially directed motion while the tab and groove combination ensures a rigid connection in the axial direction. The cantilevered locking tabs prevent rotational motion around the longitudinal axis of the setup and fix the two sides together. When the distal section is properly installed, the connector locks automatically due to the cantilevered tabs. To unlock the distal section, the user has to press both buttons at opposing sides of the proximal section while rotating the distal side anti clockwise.

The distal MTIs protrude partly into the proximal section when the sections are coupled. In order to not interfere with the proximal MTI, the distal section is engaged 15° rotated with respect to the proximal section. This is exactly between two actuation units that are spaced 30° from one another. Once coupled, the path of the tendons is co-linear with the actuation unit.

Since 3D printing will be used as manufacturing

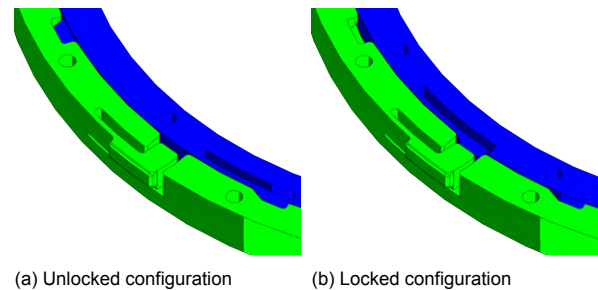


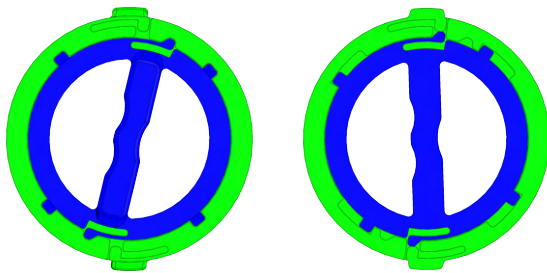
Figure 3.9: Close up of a cross section of the distal and proximal locking rings assembly. An unlocked and locked configuration is shown. The cantilevered locking features are visible. The holes in the parts receive the threaded rods for structure.

process, the locking mechanism can be designed as one unit instead of using multiple parts. The unlock buttons are located on cantilevered leaf springs meaning they are spring-loaded and move back to neutral upon release, shown in Fig. 3.9. The distal locking tab is also spring loaded as shown in Fig. 3.9 using a leaf spring in same fashion as the unlocking buttons. The distal leaves are bend when the parts are being rotated into place. When the sides are fully connected, these leaves push the locking tab into a slot in the proximal side and lock the parts together. For detaching the distal section the buttons on the proximal sides need to be pressed while rotating the distal section. This causes the spring loaded tabs from ring of the distal section to disengage from the slot in the ring of the proximal section.

A small scale connector was designed and printed as proof of concept. A small amount of filing of the distal protrusions was required to get a good fit. The result was promising as a firm fit was realised without noticeable play between the



(a) Test print of connector. The proximal ring is shown left, the distal ring is shown right.



(b) The unlocked configuration (c) The locked configuration

Figure 3.10: Test parts of the connector. The top figure shows the two printed connector parts, the bottom pictures show the unlocked and locked configurations in the Solidworks assembly. The blue part is the proximal connector part, the green part represents the distal connector part.

two parts. This locking mechanism was adapted to the test setup version.

The cantilevered parts of the rings are not printed with an extension to form a bridge. For these sections regular supports are used as the larger tabs have enough area to be printed onto supports and are easily cleaned with basic tools. Supports are sufficient because the tolerances are not critical for this part. The circumferential grooves in the ring of the proximal section (Fig. 3.9, green) have an overhang angle to improve print quality without needing supports. Tolerances are critical for this part, using supports compromises these tolerances and extra cleaning may be required.

3.2.5. Tendon tension sensor

Tension sensor concept

For the force sensor we came up with the idea of combining a spring with a distance sensor. By using a linear spring with known stiffness k and a sensor that measures the distance between the neutral and extended spring position Δx one can calculate the force F by multiplying these quanti-

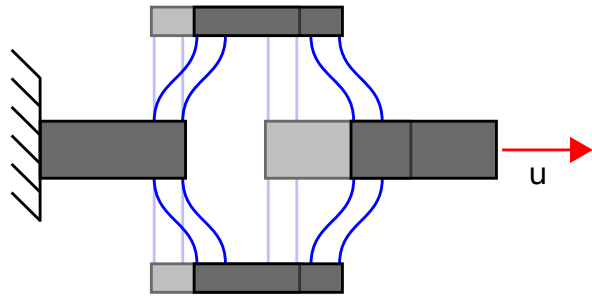


Figure 3.11: Compliant translational joint mechanism used for the spring in the force sensor. The gray colored boxes represent the stiff bars of the mechanism. The blue lines represent the flexures. The deformed state is shown in light colors and the deformed state is shown in darker colors. The direction of motion is indicated with the red arrow.

ties as indicated by Eq. (3.1).

$$F = k * \Delta x \quad (3.1)$$

This approach means that there is a slight mismatch between actuated tendon length and motor actuation length when a load is applied to the tendons. This can be adjusted for because the additional actuation displacement is measured by the sensor. The spring and distance sensor for this approach should behave linearly for simplicity. The displacement of the force sensor should be low, meaning that a stiff spring and a distance sensor for relatively small displacements need to be used.

Tension sensor spring

The principle of a linear stage is used to realize linear motion using blade flexures or leaves, this concept is visualised in Fig. 3.11. Using at least two parallel blade flexures or leaves per side the mechanism is constrained to only allow pure translation in one direction. Multiple leaves can be added per side to increase the stiffness. The leaves can be printed using FDM. A force sensor using the principle of an FDM printed spring in combination with a distance sensor has not been reported in literature at the time of writing and is worth exploring considering the low cost character. Normally one would make such mechanism using spring steel leaves which are assembled into some sort of fixture. The disadvantage of using plastics over spring steel is the viscoelastic behaviour, temperature dependence and creep. However, printing the complete part eliminates the need of manually assembling steel leaf springs which can be rather tedious and time consuming.

Dimensioning the sensor spring

The stiffness of the complete mechanism can be derived as follows. Essentially, 4 spring pairs are

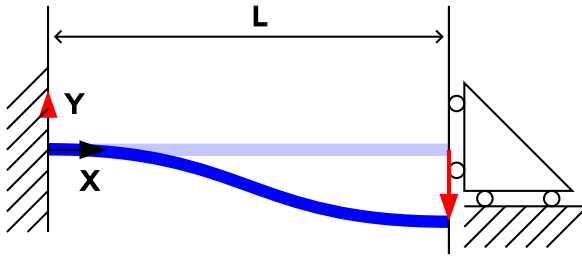


Figure 3.12: The linear beam theory model of the flexure used for the spring in the force sensor. The light blue line represents the undeformed shape or the flexure. The deformed beam is indicated by the dark blue line. The red arrow indicates the direction of deflection.

shown in Fig. 3.11 where each pair consists of two leaves. The mechanism is split in two sides, one fixed to ground and one free to translate. Each side has two spring pairs in series. The two sides together form a parallel configuration. Therefore, the total stiffness of the mechanism is the same as the stiffness of one spring pair.

The requirements state that the largest surface that can be printed is 220 mm * 220 mm as this is a common surface size for many FDM printers. The motors of the actuation units are packed tightly with only 2 mm clearance between each motor at the corners. This forces the spring design to be oriented in radial direction as can be seen in Fig. 3.4. This forms a restriction on the size of the force sensors. To keep space for the locking rings and structural rods, the length of the leaves of the spring is set to be 15 mm. The thickness of the whole sensor is set at 10 mm to fit the 3 mm diameter linear guide rods of the actuation units with enough material to retain them. Increasing the width of the leaf, and thus thickness of the print because of the way it is oriented in the printer, increases the stiffness of the springs, but also increases printing time. The thickness of the leaves is set at 0.8 mm which is the width of two printer extrusion lines using a default 0.4 mm nozzle. From the requirements follows that the maximum actuation force needs to be 50 N.

With these parameters set the dimensions of the leaf are 15 mm * 10 mm * 0.8 mm | *w*t. The deflection of a leaf can be calculated using linear beam theory formulas. The leaf is fixed at one side while the other side allows for X and Y translation, but constrains the rotation as indicated in Fig. 3.12. The formula of the maximum deflection for this situation is given by Eq. (3.2) [45]

$$\delta_{max} = \frac{F * L^3}{12 * E * I} \quad (3.2)$$

With δ_{max} the maximum deflection, F the applied force, L the length of the leaf, E the Young's modulus

and I the second moment of inertia given by Eq. (3.3)

$$I = \frac{1}{12} * w * t^3 \quad (3.3)$$

Where w is the width of the spring and t is the thickness of the spring. The Young's modulus used for printed PLA is 3.17 GPa [46]. The deflection of the spring is set to 2.5 mm to have enough deflection to be measured using a sensor. The amount of required leaves can be calculated using Eq. (3.4).

$$n = \left\lceil \frac{F}{\frac{\delta_{max} * 12 * E * I}{L^3}} \right\rceil \quad (3.4)$$

Where n represents the number of springs required for the given load F . With the numbers used as presented above, the required number of leaves is 4.

Spring design for FDM printing

Every manufacturing technique has its own advantages and limitations. FDM printing is no exception. Besides a limited range of useable materials, the process makes the printed parts highly non-homogeneous. The most noticeable effect of this shows up in the strength in different orientations. The orientation in which the model is printed can greatly impact the strength of the final product. The weakest direction is in the Z-axis or X-Z and Y-Z planes where layers are stacked on top of each other which are fused together. The strength in the X-Y plane is higher and thus preferable to have flexible parts oriented in this layer. This prevents stresses between the stacked layers during bending. The strength in a layer is stronger because the material is laid down in a continuous extrusion.

The model is sliced in vertical slices before it is printed. Each slice has at least one start and stop location at the perimeter also called outer wall which is determined by the slicer depending on the specific settings that are used. That location is visible and can introduce a weak spot the model. This spot is present in every layer, which generally form a seam in the Z direction. In most applications this will not be a problem except for aesthetics. However, with the model for the force sensor spring there are multiple of these seams as can be seen in Fig. 3.13a. Using Solidworks build in Finite Element Method (FEM) reveals that the seams are positioned at locations corresponding to the highest stresses as shown in Fig. 3.14. One could also opt to introduce rounded corners where the flexures meet the body of the part, allow the stresses to flow more easily when a load is applied. However, considering the nature of FDM printing this

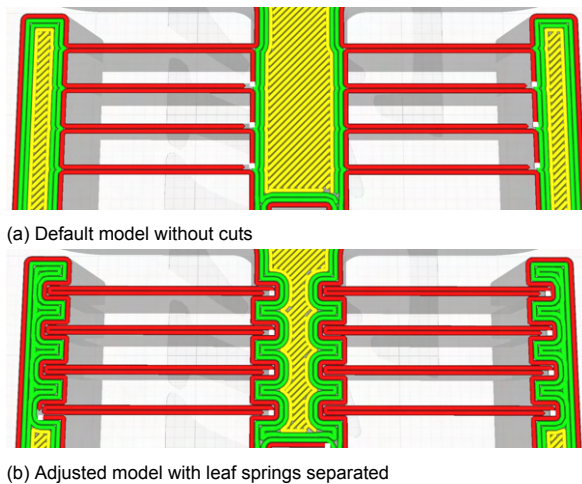


Figure 3.13: The two versions of the spring used in the force sensor sliced with Cura. The white dots indicate the starting points of the outer printed wall which is colored red.

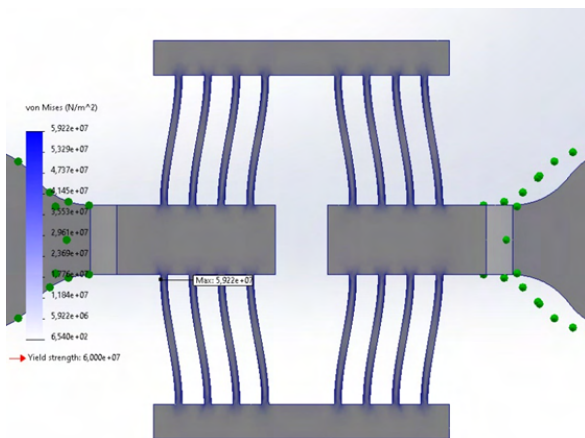


Figure 3.14: FEM analyses in Solidworks of the stresses in the spring tested in the tensile tester. The highest stresses can be found in the corners where the spring leaves are connected to the bodies.

adds non-uniformity at this spot and therefore introduces a weakness as the wall lines divert when the fillet is printed. One can alter the design of a model such that the slicer puts the seam in a different location. This was popularized by Tom Stanton on YouTube [47]. The strategy Stanton is deploying is to remove small sections of the model that causes the slicer to interpret the model as having more walls than it actually has. Nevertheless, the removed sections are so small that the walls still fuse together in the process of printing and thus keeping the strength. The leaf springs are the weakest parts and should be printed as uniformly as possible in order to optimize strength and minimize imperfections. Therefore the model is cut such that the leaves sit partly inside the rigid thicker parts which act as a comb as shown in

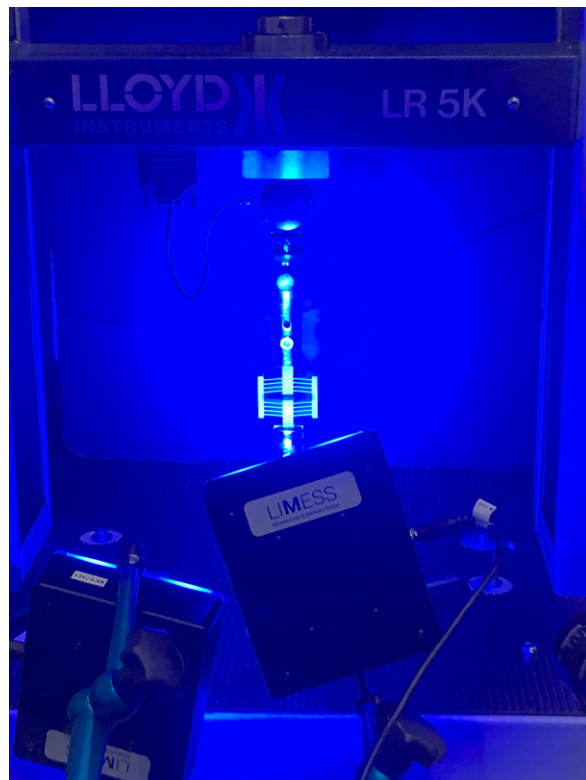


Figure 3.15: Overview of the setup used for experimentally evaluating the behaviour of the spring. A Lloyd instruments LR 5k tensile test bench with 100N load sensor is used to measure the force. A Limesse stereo camera is used to track the displacement.

Fig. 3.13b. When sliced, the Z-seams are located inside the thicker part resulting in a more homogeneous finish at the location where the stresses are the highest. The gap between the leaves and the combs is 0.025 mm. A gap as small as possible should be used to ensure proper fusion of the print lines. However, a too-small gap can result in the slicer ignoring this gap and treating the model as one solid resulting in a sliced version as shown in Fig. 3.13a.

Testing the sensor spring

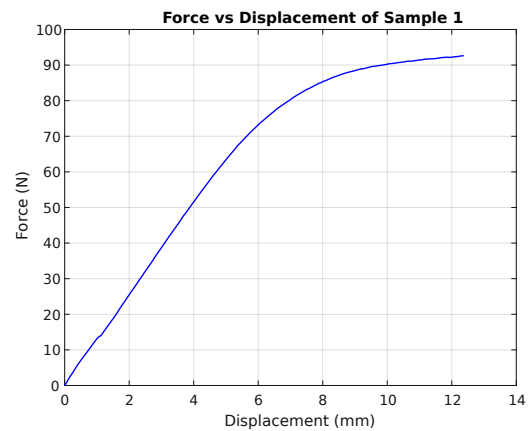
The 3D printed spring design was tested with a Lloyd instruments LR 5k tensile test bench with 100N load sensor and a Limesse stereo camera for displacement tracking. The sample was extended at a rate of 2 mm per minute. An overview of the setup with a sample is shown in Fig. 3.15. A destructive first test was performed to see when the spring fails. The first sample was extended to maximum load as shown in Fig. 3.16a. The sample did not break, but started to plastically deform around 5 mm extension. A linear response up to 4 mm extension can be seen in the graph. The other 5 samples were extended up to 4 mm and then relaxed to 0 mm extension for at least 3 times as

shown in Fig. 3.16b and Fig. 3.16c. This was done to see the effect of creep. The force displacement relation is highly linear for each of the samples. Notice the start of the graph in Fig. 3.16c where the line suddenly shifts. For the subsequent repetitions the shift is also visible. This is likely due to improper fixation of the sample in the setup. The sample possibly slips slightly in the fixation due to loose tolerances between the retention pin and holes of the sample. There is also slight decrease in maximum force visible after each extension as shown in Fig. 3.16b. This is likely to be caused by creep. When returned to zero extension, the force dips under the 0 N mark which indicates compression. This is likely caused by a combination of improper fixation and creep.

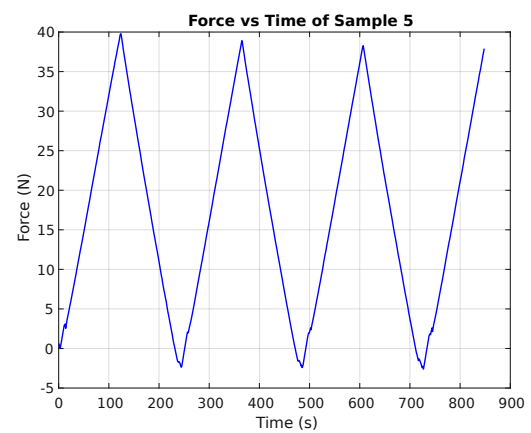
Hall effect sensor

Hall effect sensors are affordable sensors and can be used with a micro-controller without the need of an additional signal amplifier. These sensors generate a signal when exposed to a magnetic field. There exist two types of Hall effect sensors linear and digital or switch sensors. The digital sensors output either a high or a low voltage, on or off, depending on the strength of the magnetic field. When placed in a magnetic field with a value below the set value of the sensor the output will be low. However, when placed in a magnetic field with a value higher than the set value, the output will be high. This property can be used as a switch in an electronic circuit. Linear Hall sensors on the other hand output an analog voltage often between 0 V and their supply voltage, e.g. 5 V. Depending on the specifications of a specific linear sensor, a high negative field results in an output of 0 V and a high positive field results in 5 V output. The values in between depend linearly on the strength of the applied magnetic field. This sensor can be used together with a magnet to determine the distance between two moving parts.

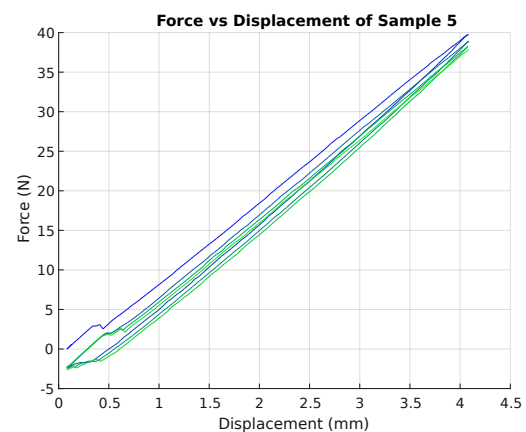
Magnets generally do not have a linear gradient of the magnetic field. However, part of the gradient is linear, which depends on the size of the magnet and the distance of the magnet to the sensor [48]. This can be experimentally established by moving the magnet relative to the Hall sensor and recording the output values of the sensor, schematically represented in Fig. 3.17. The distance d between the magnet and sensor can be adjusted in order to find the most linear region. From a set of magnets the best performing magnet was chosen to get a linear response for the required displacement. Twelve magnets of the same size were evaluated, the variation between the magnets is indicated in Fig. C.1. This was done using an experimental



(a) Force vs displacement graph of sample 1



(b) Force vs time graph of sample 5



(c) Force vs displacement graph of sample 5

Figure 3.16: Matlab plots of the tensile test data of the 3D printed spring.

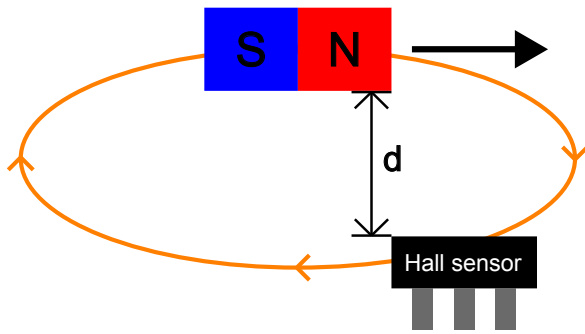


Figure 3.17: Schematic representation of how the magnet moves over the hall sensor. The distance d is experimentally determined. The black arrow indicates direction of motion. A magnetic field line is shown in orange.

setup using a 3d printed motion stage driven by a stepper motor. The output data of the Hall sensor as well as the step counts of the motor were recorded while the magnet moved over the sensor. A cylindrical magnet of height 5 mm and diameter 5 mm was found to give satisfying results at a distance of 2.0 mm from the sensor.

Final design force sensor

The final design of the force sensor is a fully 3d printed spring with a Hall effect sensor and magnet. The force sensor is directly attached to the sliding mechanism using a tight friction fit. A m3 heat set insert is pressed into the force sensor to assemble the spindle of the motor. Furthermore the proximal MTI is integrated into the spring. A small bridge is used to improve print quality and eliminates the need for supports for the overhanging structure onto which the Hall sensor is glued. The bridge needs to be removed after printing to allow the flexures to be moved. The magnet can be pressed into a slot and glued in place when properly seated. The Hall effect sensor can be glued in slot above the magnet. Note that the Hall effect sensor is attached to the proximal side of the force sensor and the magnet to the distal side. This prevents any possible strain effects of the wires attached to the Hall effect sensor to influence the measurements. For the specific magnet and Hall effect sensor used the Analog to Digital Converter (ADC) value should read around 60-70 when no load is applied. This ensures that the response of the force sensor is as linear as possible.

3.2.6. Actuation unit

Actuators

The requirements state that the test setup must be designed for 12 actuators to be used with manipulators with 3 steerable segments. It is also stated that the design must be adjustable for the number of necessary actuators when manip-

ulators with less than 3 steerable segments are tested. Therefore the tendon driving mechanism is designed with modularity in mind. A single actuation unit was designed such that it can be multiplied and arranged in a circular pattern. This also allows for a variable test setup design that can be adjusted for the number of manipulator segments.

As mentioned earlier, an electromagnetic actuator will be used for actuation. Several options such as DC motors, servos, stepper motors and linear motors can be used. DC motors need a way of position encoding in order to work with the intended use case. Servos are straightforward to control, however they have a limited range of motion. Stepper motors are also straightforward to drive and control and have unlimited range of motion. Linear motors can be quite costly and are mostly reserved for industrial applications. Therefore a stepper motor fits the needs of this project best.

A maximum distance of 100 mm has to be actuated by the test setup. When a rotary motor such as a stepper motor is used, a spool to hold the tendons is required. However, this solution has a relatively low resolution. The most abundant stepper motors have a resolution of 200 steps per revolution, or 1.8° per step. Consider a spool of 10 mm diameter, which holds 31.4 mm tendon per turn, gives a resolution of 0.16 mm per step. Of course increasing the spool diameter reduces the resolution and a smaller diameter spool increases the resolution. However, spooling a tendon means that the actuated length varies as the tendon is wound or unwound as the diameter is changing with the tendon being spooled on top of itself. Micro stepping, that is electronically increasing the amount of steps a stepper motor makes per revolution, can be used to increase the resolution. However this comes at the cost of motor torque and thus the force that can be applied on the tendons. Also a larger spool diameter requires more torque to be actuated which can be challenging with micro stepping. A reduction such as a gearbox could also be used, however this would increase the test setup costs significantly as well as introducing additional backlash. It is challenging to satisfy the resolution requirement using a rotary actuator. Linear actuation using, for example using a lead screw, can be more precise and powerful. The same stepper motor can be used which in combination with a lead screw that converts rotational to translational motion. One full rotation of the motor corresponds to a linear advancement by the pitch of the leadscrew. Such solution requires the use of a slider mechanism. Often when using these mechanisms, a carriage moves over



Figure 3.18: The slider, motor mounting plate and assembled motor are shown. An empty slot for an actuator is shown next to the mounted motor.

a slider track and the driving motor is stationary at the base of the slider. This principle would interfere with other parts of the setup. The carriage is in the neutral position, or half the actuation range, when the distal section is attached or detached. This means that half of the slider track would be protruding into the distal section, which is not possible as the slider track interferes with the twisting locking method. Therefore it is chosen to keep the motor stationary and move the whole slider mechanism, leading to the choice of non captive stepper motors.

The chosen actuator is a NEMA 11 Non-Captive Acme Linear Stepper Motor (Stepperonline Inc., NY, USA) with a 1.27 mm lead ACME thread [49]. A non-captive stepper motor has a leadscrew moving axially through the motor. Inside the motor is a nut that rotates when the motor receives power. The lead screw must be fixed with respect to an assembly, to which the motor is attached, that allows translation to prevent rotation when the motor is moving. This motor has 200 steps per revolution, thus giving a theoretical resolution of 6.4 μm per step. This motor was not provided with a linear guide to constrain the motion to pure translation. Therefore a custom guide was realised with two 3 mm circular rods that slide in a pair of bushings parallel to the lead screw and adjacent to the motor frame. A small prototype was built to check for tolerances and feasibility. Using 3D printed PLA for the bushing showed relatively low friction as the slider was easily moved by hand. 3D printing allows the bushings to be integrated with the motor mounting plate to form a single part. A mounted motor and slider mechanism can be seen in Fig. 3.18.

Position feedback

Stepper motors lack absolute positional feedback. While dead reckoning can be used to keep track of the current motor position, some external absolute reference is required to know the current position of the axis. The simplest implementation is to use a limit switch which is a very common approach in 3d printers, laser cutters, Computer Numerical Control (CNC) routers and similar machine tools. When triggered, the normally closed circuit of the switch opens which can be detected by a micro controller. In a 3D printer this is used for homing the stepper motors that drive the three axes of the machine. When starting a print, the motors will move in the homing direction until the switch corresponding to that motor is pressed. At that point, the current position of the motor is now the home or zero position from which it can move to specified positions. This principle is also used for the test setup. The motors advance until their limit switches are pressed after which the micro controller zeros the current position. Then the motors move to the neutral position where the distal section can be attached to the setup. This method is not solid, it cannot account for skipped steps of the stepper motor. Skipping steps generally occur when an external load applied to the motors is higher than the torque the motor can supply. Stepper drivers that are more advanced, and more costly, can detect skipped steps, which can be used to trigger a re-homing cycle to regain positional tracking and then be accounted for in the software. A position encoder could also be used but this adds to complexity and cost. Provided that the required load to actuate a manipulator plus friction loads is below the maximum actuation capacity of the motor, the motor should not skip steps. Therefore, it is deemed sufficient to only use low cost stepper drivers in combination with limit switches for this prototype. At the end of the slider mechanism, a bar including a stopper is attached. The stopper makes contact with the switch when the actuation unit is homed. This stopper can be adjusted by loosening and tightening a bolt to slide it along the sliders. This is needed to dial in the correct homing position of the stepper motors in order to allow proper connection of the MTIs. While this is also possible to achieve in the code of the microcontroller, having a physically adjustable stopper is more convenient. Added to the stopper is a small block with a slit. This is to hold the tendon that is attached to the Hall sensor in the force sensor and helps to guide the tendon through the motor mounting plate when the actuation unit is in motion.

Actuation units pattern

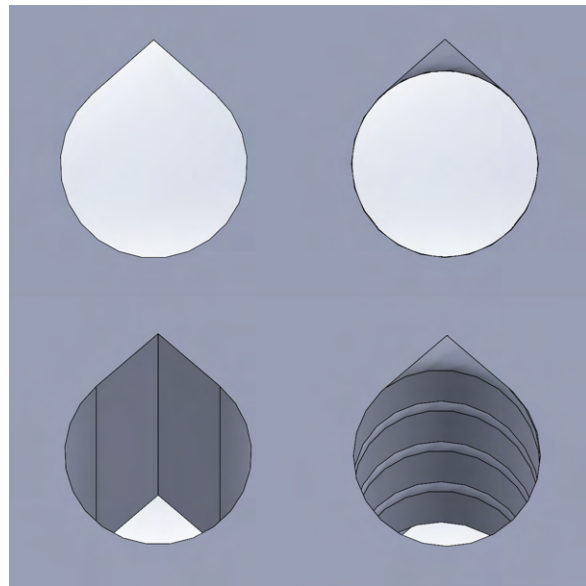
With parametricity in mind to allow for different amounts of actuated manipulator segments, the actuation units need to be oriented in an easily adjustable pattern. Also the coupling has to be taken into consideration for the pattern. As mentioned in Section 3.2.4, the connector is designed with the actuation pattern in mind. A circular pattern is chosen for the actuator units to be easily compatible with the coupler. Circular may not be the most space efficient way of arranging the units as the space in the middle of the unit is not used. However it is highly symmetrical and the design can be easily adjusted to be used with more or fewer actuators. The hollow center can be used as a pass-through for instruments to be inserted into the manipulator.

Slider bushing

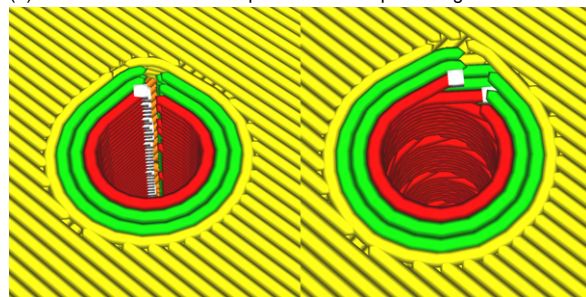
As mentioned previously in Section 3.2.1 and Section 3.2.5, a vertical seam is present when a model is sliced for printing. With a circular hole the seam is often placed based on least print time. As the print head slows down and stops near the end of the perimeter, a buildup of pressure in the nozzle can extrude some extra filament resulting in a bulge at the location of the seam. This can be an issue when vertical circular holes are printed. The bulge affects the roundness of the hole and can interfere with inserted parts, e.g. axles, sliders, etc. To accommodate for this issue, the circular hole can be altered into a teardrop shape. If the slicer z-seam location is set at corners, the bulging, happens just outside the circle in the teardrop corner. This eliminates the interference with e.g. slider parts. A possible downside of this approach is that the teardrop is not completely circular and may cause uneven sliding on the rod as there is a small gap. A simple fix is to spiral the teardrop shape with a few rotations resulting in circular tube when viewed from above as shown in Fig. 3.19a. The sliced versions are shown in Fig. 3.19b. Evenly contact with a slider is realised with this design approach. The spiralized teardrop is used for the slider bushings.

3.2.7. Structural cage elements

The sub assemblies are held together using m4 threaded rods and nuts to form a cage like structure. The mounting plate of the motors as well as the connector rings, diffuser and plate of the MTI locking are structural elements. Together with the rods, the parts form a rigid assembly able to bear the loads experienced during use. The threaded rods and nuts are low-cost and can be found in many online and brick-and-mortar stores.



(a) CAD model of the teardrop feature with top and angled views.



(b) The sliced versions of the teardrop feature.

Figure 3.19: comparison between the vertical teardrop cutout, left hand side, and the spiral teardrop cutout, right hand side. The spiral teardrop cutout has a circular profile. The white dots in the sliced part show the start and stop location where bulging can happen.

The threaded rods are easily cut to size using a metal saw, angle grinder or the like.

The rods are inserted in the coupler rings on both the distal and proximal sections. The holes for these rods in the rings are dimensioned under size so the rods self-tap into the material. Threading the holes before assembly can be done, however depending on the tolerances of the holes this is not required. All the other parts are held onto the rods using nuts. A single nut is used to sandwich the locking rings and plates together. Jammed double nuts are used at the opposing ends of the rings to set the correct distance between the mounting plate for the motors and the diffuser.

The linear guide cannot bear loads perpendicular to the plane of the guiding rods and ACME screw well. When the distal section is being attached or detached, a small perpendicular load is applied to the linear guide. A plate with cutouts for the force sensor and distal MTI was installed to

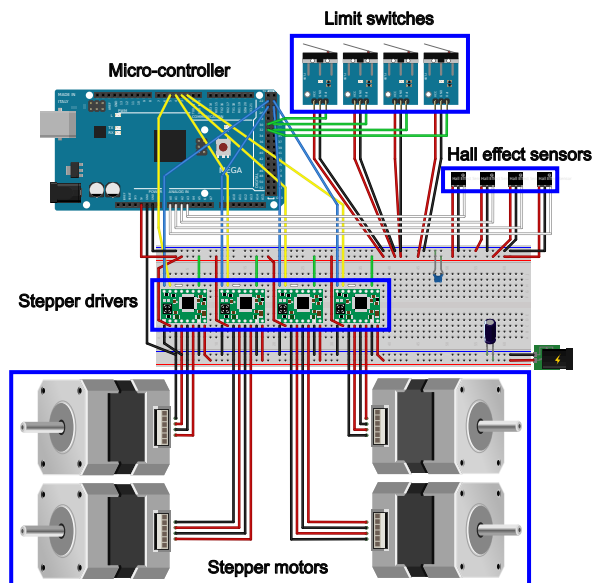


Figure 3.20: Schematic overview of the electronics used for the prototype.

hold the sensors in place during connecting and disconnecting the distal section (Fig. 3.4, white plate). The cutout in the plate has a 0.8 mm gap around the force sensor and distal MTI to allow pass through.

3.3. Prototype

3.3.1. Prototype electronics

The setup is controlled using an Arduino Mega 2560 Rev3 microcontroller. This board is open-source and has enough input and output pins to connect all the motors, limit switches and sensors. The board is supplied with 5 V DC via USB using a computer. A wiring diagram is shown in Fig. 3.20. The stepper motors are supplied with a 24 V DC Mean Well NDR-120-24 power supply. A4988 stepper drivers are used to drive the motors which are low cost and readily available. The Hall effect sensors are connected to the analog input pins of the microcontroller. They are supplied with 5 V from the microcontroller. Since the limit switches only give a high (5 V) or low (0 V) output they are connected to digital pins. Additionally a 25v 1000 μ F electrolytic capacitor is placed on the power rail for the motors to smooth peaks in voltage during operation. A 50 V 220 nF ceramic capacitor is placed on the power rail for the Hall sensors to filter high frequency noise.

3.3.2. Prototype software

The Arduino microcontroller runs on the Arduino coding language which uses the C and C++ language as a base. On the computer a Matlab pro-

gram gathers the data gathered by the microcontroller to be processed further. The user can modify these program for their specific needs. What follows next is the program used for this setup.

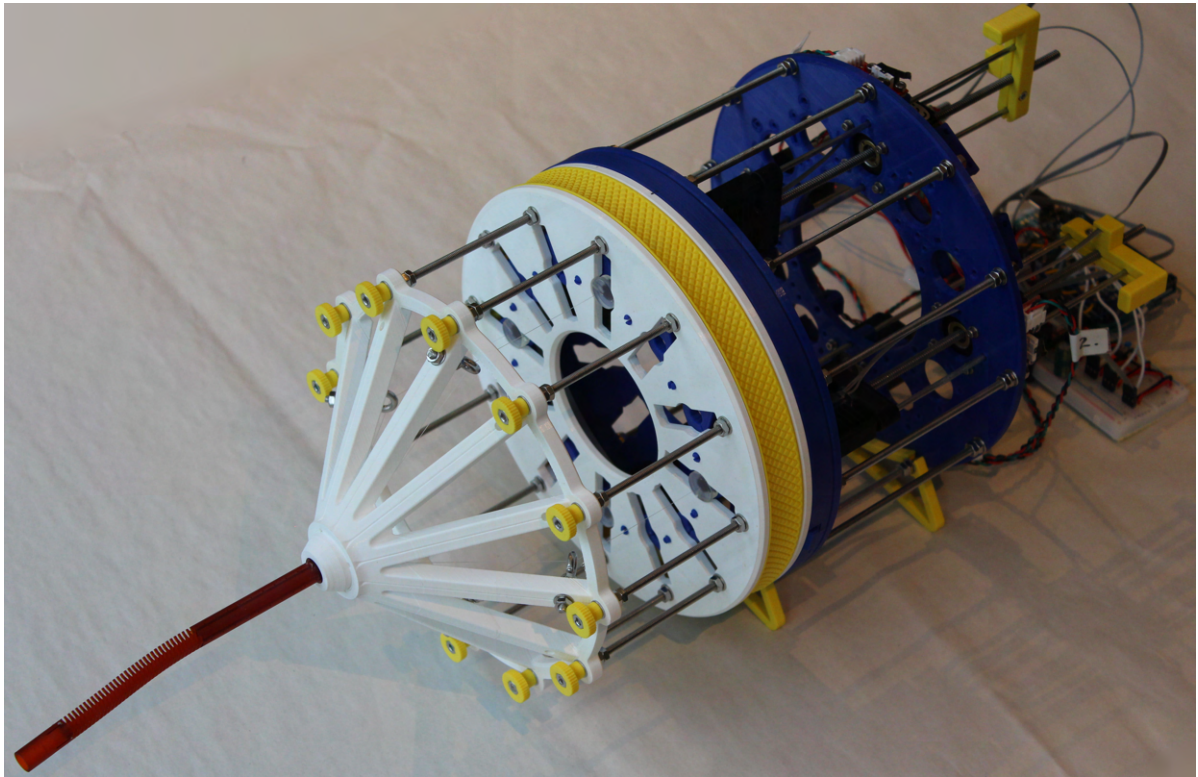
The programs are structured as follows: First the Arduino program needs to be uploaded to the microcontroller. Then the Matlab script can be run where the user can specify a folder name to save the data and graphs produced by the Matlab program. Followed by specifying the radius at which the tendons are located in the manipulator and the requested deflection in degrees. These numbers are converted to the number of steps the motors have to move to realise the requested deflection. A handshake is made between the microcontroller and Matlab after which the microcontroller homes the actuation unit. This is done by moving all stepper motors until their respective limit switches are activated after which they move to a predefined location to enable the installation of the distal section into which the manipulator is installed. Then Matlab pops up a message asking if the distal section is attached properly. The user needs to attach the distal section and make sure the connection is secure. When the user confirms the installation of the distal section, the microcontroller proceeds to pretension the tendons. A rigid tube should be placed over the manipulator keeping the manipulator straight and constrain any motion during the pretension sequence. Tendons can differ in length due to manual installation and the pretension sequence aims to remove any possible slack. A new popup is displayed on the screen when the pretension is completed, asking if the user is ready to start the test sequence. The tube must be removed before confirming the popup, as testing commences immediately. Matlab sends the amount of steps to move each motor to the microcontroller and the test sequence starts. First motor 1 pulls and its antagonist motor 3 eases until the amount of steps are reached. This position is held for 3 seconds after which the motors return to their original location. Another 3 seconds pass which are proceeded by actuation the next motors in the same manner. This is repeated until each tendon is pulled. The raw sensor data as well as the test runtime and stepper location is send to Matlab while the test sequence is running. The test is now completed and the motors return to home, enabling the user to disconnect the distal section if necessary. Matlab creates plots of the gathered data and saves the data in the folder specified at the start of the program.

The proposed programs are by no means set in stone. This program is meant to showcase a possible test sequence based on four actuators.

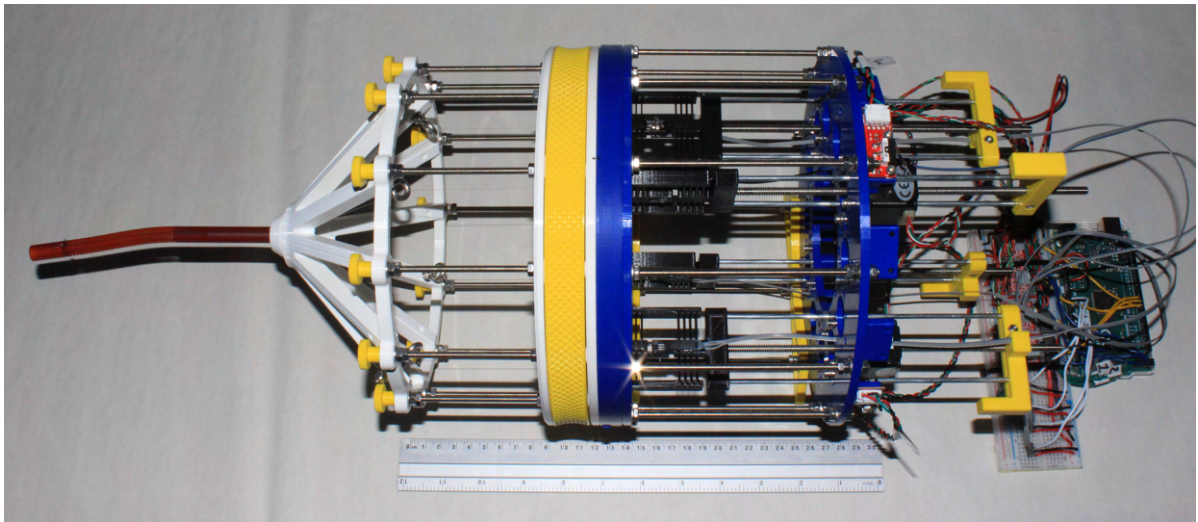
Based on the users requirements the programs can be adjusted to perform different motion cycles or even be interactive using a joystick for example. The raw ADC values from the microcontroller can be translated to force values. A calibration for each load cell is required. By hanging different weights with known masses and recording the ADC values one can fit the data to e.g. a 3th order regression. At least 4 data points are required for a 3th order polynomial fit. For the load cells used in this thesis the following values are used: Zero load, 0 g, 506 g, 1005 g, 1480 g, 2139 g, 2477 g, 2961 g, 3433 g and 3991 g.

3.3.3. Final prototype

The completed assembly of the final prototype is shown in Fig. 3.21 There are no deviations from the design other than four equipped actuator slots instead of 12, meaning one segmented manipulators can be tested. The custom parts are printed on modified Creality ender 3 printers using Cura as the main slicing software. The parts are printed with 3 walls thickness, 1.2 mm, for a balance between strength, material use and print time. 123-3D's Jupiter series PLA in various colors was used as printing material. Off the shelf parts were ordered online via various suppliers. The threaded rods were cut to size using an angle grinder. To assemble the setup the steps described in the manual provided in Appendix B were taken. A video of the prototype in action was uploaded to YouTube [50], the design files and scripts are uploaded to 4TU.ResearchData [51] and GitHub [52].



(a) Overview of the prototype.



(b) Side view of the prototype with a 30 cm ruler below it.

Figure 3.21: The final prototype assembly including an installed manipulator. Note that only 4 actuator slots are equipped with actuators and sensors to actuate a one segment manipulator.

Prototype performance

4.1. Procedure

4.1.1. Force sensor calibration procedure

First the force sensors were calibrated using a number of known weights. This is how the user would calibrate their sensors without requiring expensive equipment such as a load cell. A polynomial regression was performed that relates the ADC value from each sensor connected to the microcontroller to a force in Newtons. The accuracy of these fits was determined by calculating the error between the calibration fit and the force values retrieved from a test with a calibrated Futek load cell. The test with a Futek load cell was performed by applying tension to the sensors with each motor until a specified ADC value is reached, after which the motor moves back to starting position.

4.1.2. Flexure displacement calibration procedure

As the motors pull on the tendons of a manipulator, the flexures of the tension sensor deflect as the load increases. This deflection needs to be known in order correct the actuated distance of the tendons of a manipulator. The microcontroller keeps track of the actuated distance via dead reckoning. However this distance is the actuated tendon length plus the deflection of the tension sensor. To find the relation between ADC values and deflection of the sensor, the sensor was again fixed at one end and moved until a certain ADC value was reached. A polynomial regression relating these values was used to convert ADC to deflection in mm.

4.1.3. Flexure and Hall effect sensor hysteresis procedure

The hysteresis of a system shows the effect of direction dependency. An example graph of hysteresis is shown in Fig. 4.1 Hysteresis causes the output of the sensor to depend on the direction in

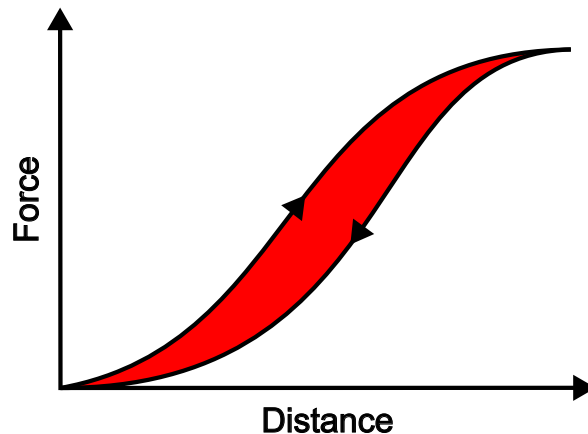


Figure 4.1: Example plot of a hysteresis loop. The red area is the energy lost in the system due to hysteresis.

which the sensor moves. Meaning that there can be a difference in sensor output for the same extension, which depends on if the sensor is extending or contracting. The data of the test with the Futek load cell will also be used to calculate this effect. By adding and removing load on the flexure, the difference can be determined and direction dependency can be demonstrated.

As with the flexure hysteresis, it is also important to investigate the hysteresis of the Hall effect sensor to be able to determine the performance of the sensor system as a whole. This can be determined by evaluating the ADC values retrieved from the same test as the flexure hysteresis.

4.1.4. Hysteresis of prototype

The hysteresis of the complete prototype was not assessed. Friction between the tendon and tendon diffuser possibly can also cause hysteresis effects. However, this depends on the specific material used for the tendons. Friction is a complex phenomenon depending on many parameters such as roughness of the materials, applied load and actuation speed. Small deformations of parts in the prototype under load also potentially add to

hysteresis effects. However these deformations, apart from the tension sensor, are assumed to be negligible when the prototype is subjected to maximum loads of 40 N.

4.1.5. Manipulators test procedure

To help determining the ability of the system to perform the task of controlling tendon-driven manipulators, two different manipulators were tested on the prototype. The manipulators were actuated in a predefined motion sequence and the data gathered by the micro controller was stored on a computer and graphed.

4.2. Materials and methods

4.2.1. Force calibration method

The following masses are used for the calibration of the force sensor: 0 g, 506 g, 1005 g, 1480 g, 2139 g, 2477 g, 2961 g, 3433 g and 3991 g. These weights include the 6 g weight of the MTI used to attach the masses to the force sensor and are measured using a kitchen scale accurate to ± 1 g. The masses were chosen in increments of about 500 g for which various weight plates and calibration weights were used. The setup was vertically positioned while the masses were attached as shown in Fig. 4.2. It was ensured that the force sensors were free from any obstructions that could interfere with the measurement. The ADC values for each sensor resulting from each weight were read from the serial monitor and noted down.

For the accuracy tests a Futek 10lb. load cell calibrated at 40 N in combination with a National Instruments DAC NI USB 6008 and LabVIEW 2018 were used. The test procedure started by attaching the load cell to the test setup making sure no pretension is measured by checking the output of the Futek load cell on a computer. Then the zero load ADC value of the tension sensor is measured on the microcontroller of the prototype. This zero load value is increased with 800 to be the target value for the microcontroller to move the motors to. The addition of 800 points to the base ADC value was determined to be below the maximum deflection range of the force sensor. From a previous experimental test it was found that 800 ADC points corresponds to just below 40 N. The motors move with constant speed, 50 steps per second or 9.5 mm per minute, until the target tension sensor value is reached after which it returns to the starting position with the same speed. During this sequence the time on the microcontroller, the ADC value of the sensors and the step count of the stepper motor is logged at 20 Hz and send to the computer where it is saved to be processed. LabVIEW

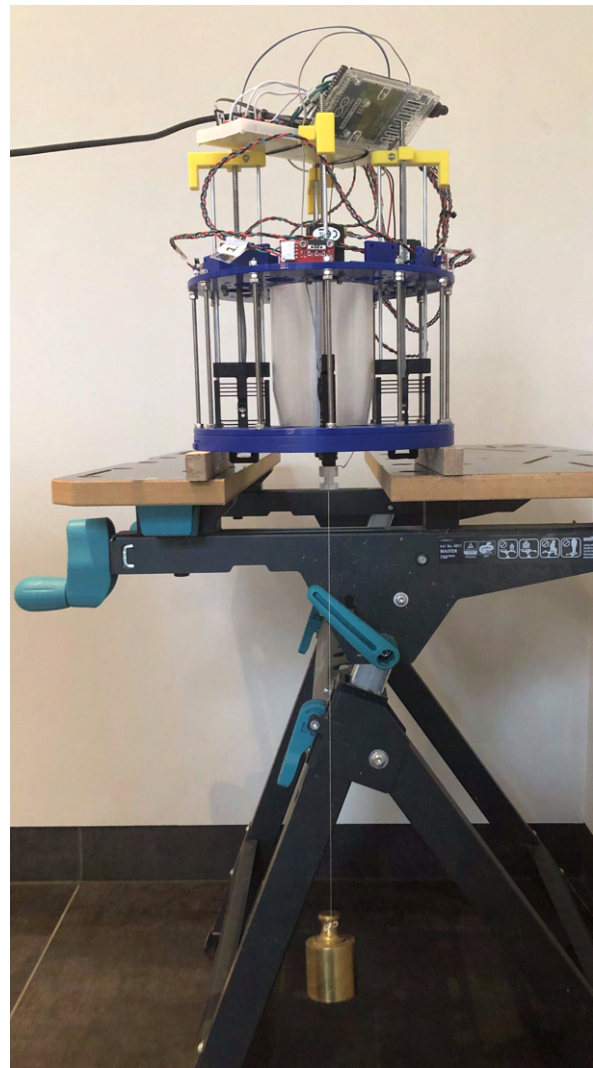


Figure 4.2: The sensor calibration setup used to gather the ADC values for each weight and sensor. The test setup was vertically positioned on a workbench. A 506 g mass can be seen hanging from the sensor, this includes the weight of approximately 6 grams for the MTI used to attach the mass to the sensor.

was used to log the time and force measured by the Futek load cell at 10 Hz and save these values. Each sensor was tested three times in a non-consecutive order. The sequence began with Sensor 1, followed by Sensor 2, Sensor 3, and Sensor 4. After completing a round of tests, this sequence was repeated in the same order. This process was continued until each sensor had been tested three times. An overview of the test setup with the Futek sensor is shown in Fig. 4.3. It was assumed that the displacement counted on the microcontroller was correct and that the motors did not skip steps during the tests.

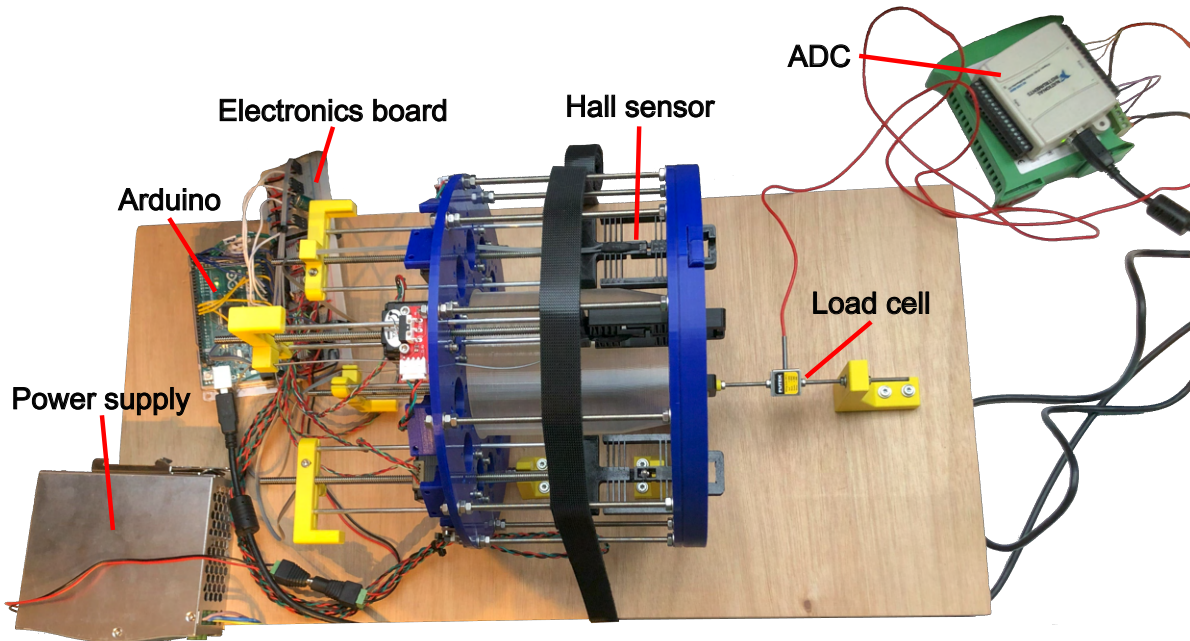


Figure 4.3: Overview of setup used to test the force sensors with a Futek load cell.

4.2.2. Flexure displacement calibration method

For this evaluation the same test and data was used from the tests with the Futek load cell. It was assumed that the the distal end of the sensor is fixed in place and that only the proximal end is subjected to displacement. The deflection of the force sensor is measured by the Hall effect sensor.

4.2.3. Flexure and Hall effect sensor hysteresis method

The hysteresis calculation also makes use of the same test with the Futek load cell described in Section 4.2.1.

4.2.4. Manipulators test method

Two different manipulator designs were tested on the prototype test setup. The first manipulator was based on the designed of the 3Flex by Trauzettel et. al. [53] and printed in white PLA. The second manipulator was based on the design of the HelicoFlex by Culmone et. al. [54] and was printed in envisionTEC R5 Red photo-polymer. Both manipulators are shown in Fig. 4.4 The manipulators were moved from the neutral position to 90° with an acceleration of 500 steps per second², a constant speed of 400 steps per second, deceleration of 500 steps per second² and held for 3 seconds. Subsequently the manipulator was moved back to neutral in the same fashion and held for a further 3 seconds before moving the next tendon. This was

Table 4.1: This table shows the third order fit polynomials retrieved from the fitted calibration of each force sensor. Where x is the ADC value and the output is the force in N

| Sensor # | coefficient a | coefficient b | coefficient c | coefficient d |
|----------|---------------|---------------|---------------|---------------|
| 1 | 3.2408e-08 | -5.0542e-05 | 0.070267 | -5.0305 |
| 2 | 2.7563e-08 | -4.5618e-05 | 0.069355 | -4.9955 |
| 3 | 2.6481e-08 | -4.1473e-05 | 0.065981 | -3.8908 |
| 4 | 2.7231e-08 | -4.3284e-05 | 0.066967 | -4.5452 |

repeated for each tendon in the manipulator.

4.3. Results

4.3.1. Force calibration results

The masses used to calibrate the force sensors were converted to Newtons by multiplying with the gravitational constant of 9.81 m/s^2 and dividing by 1000 to convert grams to kilos. Then the ADC data was fitted using a third order polynomial fit for each sensor. The fit and data points used for the fit are shown in Fig. 4.5. The constants of the third order polynomial for each sensor are shown in Table 4.1, and were implemented as shown in Eq. (4.1).

$$y = ax^3 + bx^2 + cx + d \quad (4.1)$$

Where y is the force in newtons, the constants a , b , c and d are from Table 4.1 and x is the ADC value retrieved from the sensor.

The accuracy of the manual calibration fit can be evaluated using the baseline values of the Futek measurements. However, there is a difference in sample rate between the data from the tension

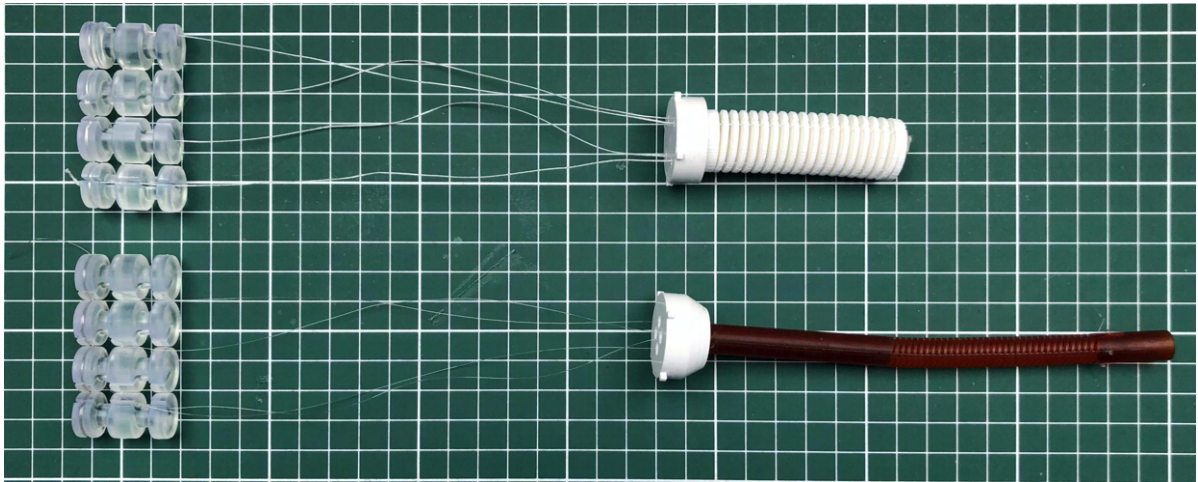


Figure 4.4: This picture shows the manipulators based on the designs of the 3Flex and HelicoFlex respectively top and bottom. Also the adaptors, tendons and distal MTIs are shown assembled.

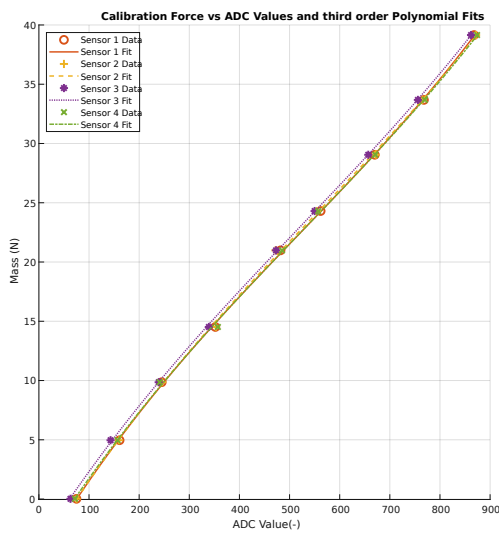


Figure 4.5: This figure shows the data points of the masses used for the calibration of the tension sensors. The third order fit through these points for each sensor is also shown.

sensor and the Futek sensor, and the recordings' starting times differ. Therefore, the data of the Futek sensor was time shifted and resampled by interpolation to match the number of data points in the tension sensor data for further processing. The ADC values of the tension sensor are converted to Newtons using Eq. (4.1) and the constants from Table 4.1. Then the difference between the Futek force values and the fitted tension sensor values was taken, which yielded the calibration error. The resulting errors for the sensors are shown in Fig. 4.6. Here the error in N is plotted against the ADC value of the sensors. A more detailed figure for each individual sensor is shown

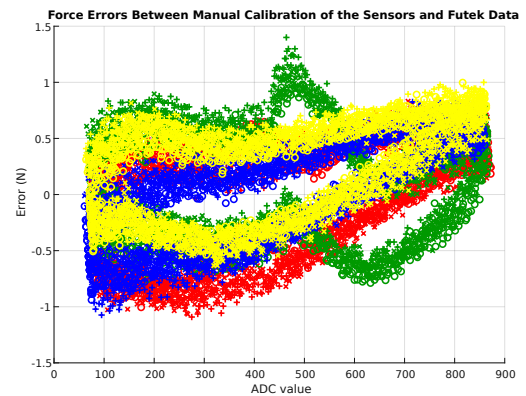


Figure 4.6: This figure shows the error in Newtons as a function of the ADC values for each sensor and each test. Each sensor data is plotted with a unique color. Red is sensor 1, green is sensor 2, blue is sensor 3 and yellow is sensor 4. Each of the three tests within a sensor is indicated with a different marker.

the appendix in Fig. C.2. The combined errors of each sensor are shown in the box plot in Fig. 4.7. Here the error distribution is plotted for each sensor. The maximum deviation from the calibration fit is 1.40 N.

4.3.2. Flexure displacement calibration results

The relation between ADC and distance values is shown in Fig. 4.8. A third order polynomial fit through all the data points of the tests combined per sensor was used to get a conversion formula to convert the ADC values to mm. The polynomial constants resulting from the fit are shown in Table 4.2. Equation (4.1) was also used here, where y was the deflection of the sensor in mm, the constants a , b , c and d are from Table 4.2 and x was

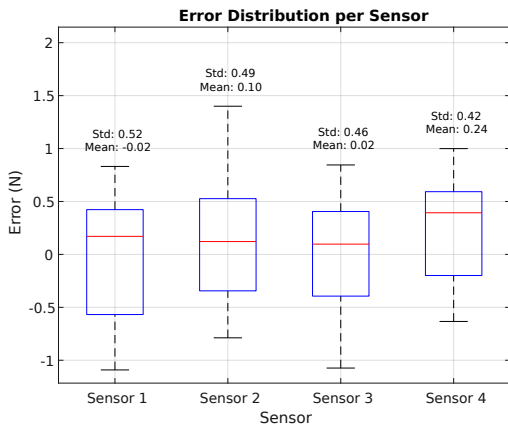


Figure 4.7: This figure shows the force error box plots of all the test combined per sensor in Newtons. The mean and standard deviation are also shown. The red bar is the median of the values. The blue bounding box represents the lower 25th percentile up to the 75th percentile. The whiskers represent the lowest and highest values within 1.5 IQR of the blue box.

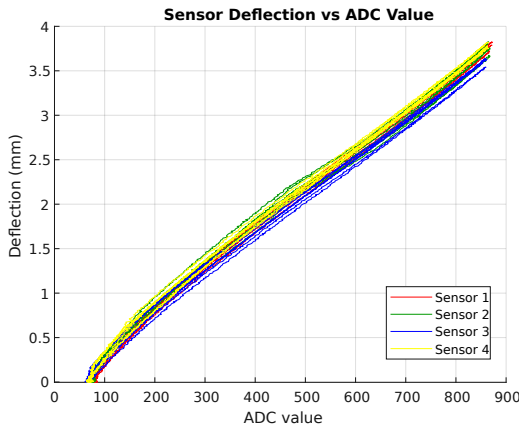


Figure 4.8: This figure shows the relation between the deflection of the flexure of each sensor.

the ADC value retrieved from the sensor. The ADC values were then converted to mm using the respective formula for each sensor and subtracted from the counted distance from the microcontroller to retrieve the fit error of each sensor. The error versus distance relation is graphed and shown in Fig. 4.9. The errors for each sensor can be found in the appendix in Fig. C.3. The combined deflection errors of each sensor are shown in the box plot in Fig. 4.7. Here the error distribution is plotted for each sensor. The maximum error is 0.147 mm for sensor 4.

4.3.3. Flexure hysteresis results

The flexure hysteresis was calculated from the data gathered from the Futek load cell and the force sensor. First the displacement was matched with the data from the Futek load cell. Then

Table 4.2: This table shows the third order fit polynomials retrieved from the relation between the ADC values and the travelled distance.

| Sensor # | coefficient a | coefficient b | coefficient c | coefficient d |
|----------|---------------|---------------|---------------|---------------|
| 1 | 3.5694e-09 | -5.9156e-06 | 0.0073457 | -0.38784 |
| 2 | 4.8409e-09 | -7.9353e-06 | 0.0081416 | -0.38054 |
| 3 | 3.9236e-09 | -6.2554e-06 | 0.0072114 | -0.38289 |
| 4 | 3.7069e-09 | -6.0364e-06 | 0.0073115 | -0.30758 |

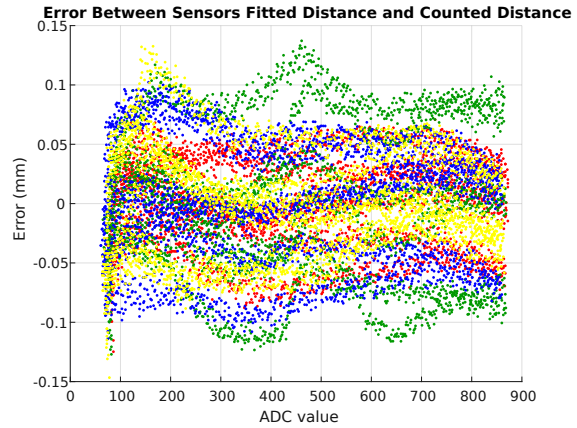


Figure 4.9: This figure shows the error in extension between the fitted ADC values and distance counted on the microcontroller in mm as a function of the ADC values for each sensor. Data from each sensor is plotted with a unique color. Red is sensor 1, green is sensor 2, blue is sensor 3 and yellow is sensor 4.

the hysteresis area, which is the area between the loading and unloading curves as indicated in Fig. 4.1. The area under these curves was calculated using the trapz function in Matlab. This function numerically integrates the Force values from the Futek load cell over the traversed distance using the trapezoidal rule. Next, the unloading area was subtracted from the loading area resulting in the hysteresis area. This value was divided by the loading area and multiplied by 100 to get the hysteresis expressed as a percentage of the strain energy. This was done for each individual test after which the mean percentage per sensor was determined. These percentages are shown in Table 4.3 The mean flexure hysteresis ranges between 5.19% and 6.43%.

4.3.4. Hall sensor hysteresis results

The Hall sensor hysteresis was calculated from the ADC values of the microcontroller. Basically the same method was used as for the flexure hys-

Table 4.3: The mean hysteresis per sensor in percentage of strain energy.

| Hysteresis Flexure | Sensor 1 | Sensor 2 | Sensor 3 | Sensor 4 |
|--------------------|----------|----------|----------|----------|
| | 6.01% | 6.43% | 5.19% | 5.74% |

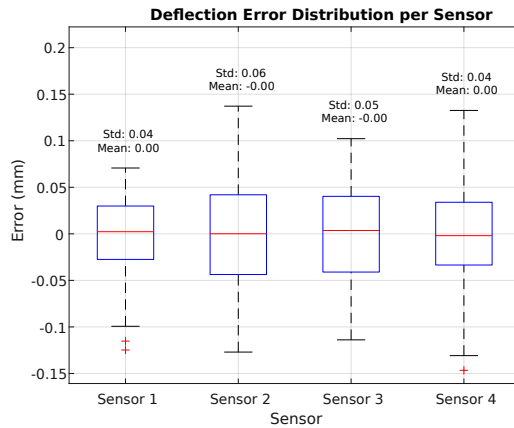


Figure 4.10: This figure shows the deflection error box plots of all the tests combined per sensor in mm. The mean and standard deviation are also shown. The red bar is the median of the values. The blue box represents the lower 25th percentile up to the 75th percentile. The whiskers represent the lowest and highest values within 1.5 IQR of the blue box.

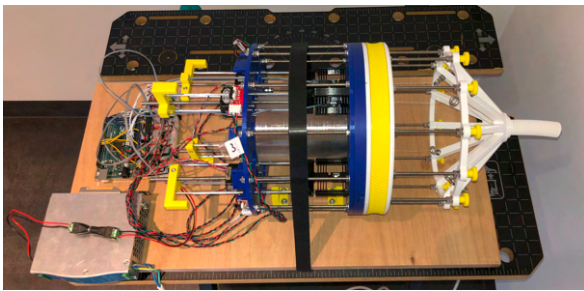
Table 4.4: The mean hysteresis per Hall effect sensor in percentage.

| Hysteresis | Sensor 1 | Sensor 2 | Sensor 3 | Sensor 4 |
|-------------|----------|----------|----------|----------|
| Hall sensor | 1.30% | 1.86% | 2.01% | 2.11% |

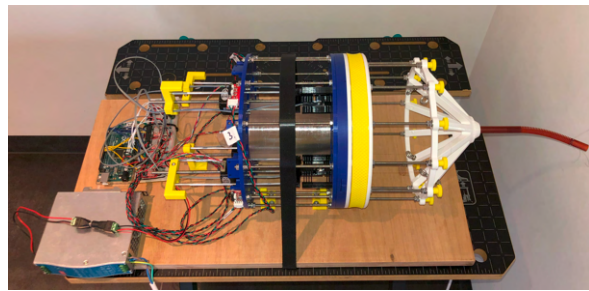
teresis, except using the ADC points in stead of the force values. The area under the loading and unloading curves are again determined using the trapz function in Matlab. These areas are subtracted and divided by the loading area and multiplied by 100 to express in percentages. The raw ADC values are used in this calculation. The Hall sensor hysteresis values per sensor are shown in Table 4.4 The mean Hall sensor hysteresis ranges between 1.30% and 2.11%.

4.3.5. Manipulators test results

An overview of the test setup with the attached manipulators is shown in Fig. 4.11. The results of these test with the Helicoflex and 3Flex based designs is shown in Fig. 4.12 and Fig. 4.13 respectively. Here both the time vs force and distance vs force are plotted. The ADC output of the Hall sensors are converted to N using the calibration fit described in Section 4.1.1.

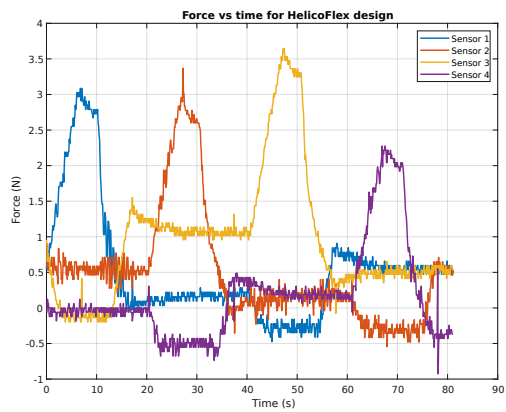


(a) 3Flex based design

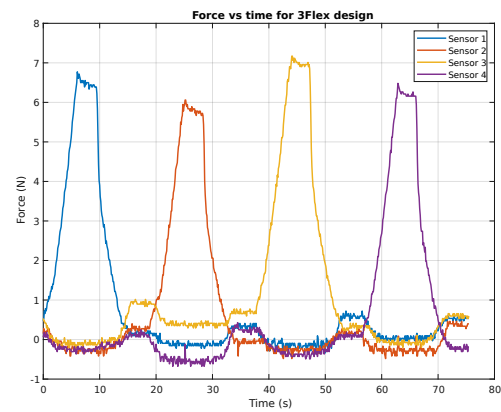


(b) HelicoFlex based design

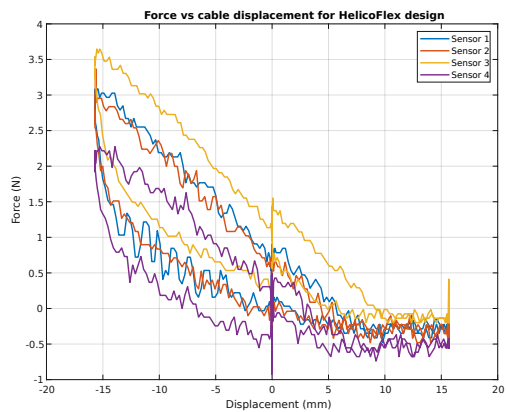
Figure 4.11: This picture shows the tested manipulators attached to the test setup.



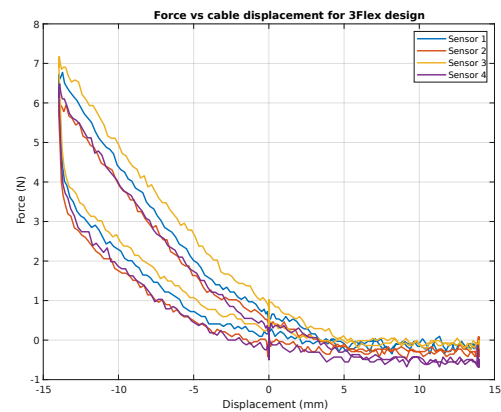
(a) Force vs time plot.



(a) Force vs time plot.



(b) Force vs displacement plot.



(b) Force vs displacement plot.

Figure 4.12: Results of the test with the HelicoFlex based design. A negative and positive displacement mean pulling and easing respectively.

Figure 4.13: Results of the test with the 3Flex based design. A negative and positive displacement mean pulling and easing respectively.

Discussion

5.1. Prototype performance

5.1.1. Force calibration

The third order fit fits the calibration points well, as shown in Fig. 4.2. However, the error clearly depends on adding and removing loads on the force sensor sensor (Fig. 4.6). The force reading from the force sensor, converted from ADC to Newtons, is lower than the actual force applied when the load increases. When this load is removed, the force reading is higher than the actual applied force as shown in Fig. 4.6. Therefore, there is an error dependency on pulling and releasing for all the sensors. The trend of the error graphs between the sensors is generally following the same shape. However, sensor 2 stands out by showing peaks in the pull and release curves, causing relatively high whisker in the error distribution of Fig. 4.7. This is observed in all of the three tests and happens around the same ADC values, between 400 and 600. Because this happens reliably for each of the three tests, it is likely caused by a small defect in the Hall sensor. It is unlikely to be caused by a problem with the flexures because the force reading does not show a deviation in the course of the graph. Sensor 1 has a small deviation around 350 and 450 in the pull and release direction for the first test. This is not systematic as the data of sensor 2. It may have been caused by the fixture of the Futek sensor or by an internal factor of the prototype.

The third order polynomial fits of the force sensors have coefficients that are relatively close to each other. This shows that the behaviour of the force sensors are similar to one another, as can be seen in the graphs. However, there are noticeable differences in actual force conversion between the sensors and therefore each sensor should always be calibrated separately. These differences can be seen in the error plots and error distributions as it varies between the sensors. The error can be up to 1.4N which is 3.5% of the total force range.

5.1.2. Hysteresis

Flexure displacement calibration

The relation between ADC values and displacement is apart from the lower end of the graph fairly linear as shown in Fig. 4.8. All sensors follow the same general shape. Sensor 2 again shows some deviation in the shape between 400 - 600 ADC. The magnets used for the force sensors are too short for the range of motion required to reach 40 N. This meant that in order to satisfy this range, the magnets are already offset to the Hall effect sensor to remove part of the nonlinear start of the graph. That is why the ADC value starts around 60-70 for the sensors. It is clear that this offset could have been increased in order to get a more linear response at the bottom end of the graph. However this could have introduced a nonlinear effect at the higher end of the graph.

The box-plot shown in Fig. 4.10 shows that the errors of the third order fit of the ADC vs deflection is distributed mostly evenly around zero. There is variance between the sensors which can be caused by variance in the Hall effect sensors and especially by the strength of the magnets. The error of the fit can be up to 0.15 mm which is rather high compared to the theoretical step resolution of 3.18 μm with half stepping enabled on the stepper motor drivers.

Flexure hysteresis

Table 4.3 shows a significant hysteresis effect of the sensors. This hysteresis is most likely caused by the viscoelastic property of the PLA material used for the printed flexures. PLA, like many polymers, exhibits creep when subjected to load, consequently lowering the force required maintain a deflected position. However, when the load is removed and the flexure gets time to reset, the force-distance relation seems to be unchanged. This is indicated by the error plots in Fig. 4.6 where multiple test runs overlap each other within the same sensor, suggesting that the sensors are not undergoing plastic deformation. There is some variance

in the hysteresis between the flexures. This is to be expected as 3D printing in general, especially on hobby grade FDM printers, has challenges producing repeatable prints of the same quality and properties. The variance can be caused by many parameters including environmental humidity and temperature, general filament quality and airflow in the room.

System hysteresis

As mentioned in Section 4.1.4 the hysteresis of the complete prototype was not identified. However, it is possible that hysteresis is introduced by the interaction of the tendons with the guides in the distal section and deformations of the prototype. As mentioned before, investigating the effect of friction between the tendon and the tendon guides requires extensive testing with a variation of applied loads and speeds for a given tendon material. Different tendons materials and roughness also have different effects on the generated friction. The deflection of the structural parts of the setup was assumed to be negligible and not contributing to hysteresis. Therefore, no system hysteresis evaluation was conducted.

5.1.3. Hall effect sensor hysteresis

There were no specifications found on hysteresis effects in the sensor data sheet [55]. However the sheet mentions an error of 6 mV peak to peak noise. The ADC sensitivity of the microcontroller is 4.88 mV per step. This means that the expected variation given a constant magnetic field is plus minus 1-2 ADC points. However, the difference between the loading and releasing curves are higher than the expected noise. Also the curves repeatedly show the same general shapes. For the same extension of the flexures, and therefore same applied magnetic field on the Hall effect sensor as these are fixed to one another, the same ADC reading is expected plus minus the noise. Therefore, the method of mounting the setup and the Futek load cell and possibly some internal factors are likely to have had an effect on this value. The actual hysteresis of the Hall sensor can be experimentally investigated using a precision motion stage that moves a magnet over the Hall sensor. This eliminates external factors such as deformations in the setup caused by loads which could have influenced the data. Though, this test was not conducted for this thesis. The sensor output and the position of the magnet is recorded while the magnet is moved over the sensor.

5.1.4. Hall effect sensor noise

The ADC output of the microcontroller has noise as can be seen in Section 5.1.3. A capacitor was placed on the sensor power rail, however noise was still noticeable. Shielded electrical wires and higher value capacitors could help reduce the noise caused by external electric fields. The data could also be filtered digitally on the microcontroller, however this cost a lot of calculation power which can cause the actuation of the setup slow down and stutter. A higher sample rate could also be used to send the data at a higher frequency to the computer and use a computer script to filter the data with e.g. a moving average. However, sampling and sending data at a higher frequency also slows down the speed of the script. Using a separate microcontroller for only the sensors and one only for the motors can be used to eliminate this issue.

5.1.5. System backlash

The non-captive stepper motors uses a lead screw and nut to convert rotational motion to linear motion. Tolerances between the screw and nut add backlash to the system. However, if there is always tension on all of the manipulator tendons, the backlash caused by the tolerance between screw and nut is likely to be negligible. The pre-tension only at the start of the test sequence is not enough. The antagonistic tendon pairs move the same number of steps but in opposing directions when the manipulator is actuated. The non perfect manipulators causes the to be actuated tendon length to differ between two antagonistic tendon pairs. This causes slack in the easing tendon. A PID control loop should be implemented to constantly monitor the tendon tension and move the actuators such that a fixed tension value is held. Note that this likely slows down the microcontroller as extra calculations need to be performed during the test sequence.

5.1.6. Manipulators test

The manipulators were successfully tested. However, some issues were identified. The noise of the sensors is particularly noticeable when more compliant manipulators are tested as can be seen in Fig. 4.12 compared to a stiffer manipulator as in Fig. 4.13. A problem with the coupling of the MTI was found, which is discussed further in Section 5.2.3. The tendons that eased during the test procedure became slack as discussed in the previous subsection. This did not cause any entanglement of the tendons with other parts of the setup. The actuators had to be watched closely to ensure that the force sensor assemblies could move freely

through the plates of the setup as discussed in Section 5.2.7. The structural coupling performed well, the distal section stayed tightly fixed during the test and was decoupled successfully after.

5.2. Design evaluation & improvements

5.2.1. Manipulator adaptor

The presented manipulator adaptor for the tendon diffuser is purely made of plastic. As the tendons slide over the plastic, friction causes losses and possibly wear when used for extended periods of time. An improved guide should be used to reduce the friction and wear of the part. A simple polished metallic ring could be installed at the location where the tendons exit the adapter. This way the tendons can slide with less friction compared to the plastic. The friction depends on the specific material used for the tendons of the manipulator. Also using a different type of material for the adaptor can influence the friction. No further tests were conducted to find the effect of friction between the adaptor and the tendons.

5.2.2. tendon diffuser

The tendon diffuser part was, unlike the other FDM printed parts, not sliced in Cura. Cura did not slice the part as was envisioned beforehand, with the print seams located in the ridge of the spokes. The "Sharpest Corner" setting in Cura did not work reliably as some spokes had the seam elsewhere than in the ridge. Therefore, Prusa Slicer was used for this part. This slicer has the option to manually 'paint' the location of the seam. The ridges were manually painted and the model was sliced nicely. A different tendon diffuser design or a more FDM optimized spoke design may fix this minor issue.

5.2.3. Motion transfer interface MTI coupling

An issue occurs when the distal section is attached to the proximal section. The distal MTI do not always properly engage with the proximal MTI. This is likely due to a combination of the loose tolerance of the actuation sliders, too wide tolerance gap between the force sensor and cutouts in the plates, and the force that needs to be overcome when the MTIs engage. To engage the MTIs, a slight force needs to be overcome due to the spring loaded pall that holds the distal MTI in place when it is properly attached. This force is pointing lateral against the sliders. The loose tolerance of the slider mechanism allows the sensor to move lat-

eral in the direction that the MTIs engage, which is unwanted. The the plates through which the force sensor moves should limit this movement, however the gap is too large to allow for proper engagement of the MTIs. The solution for now is to manually check the connection of the distal MTI and adjust if necessary. This issue could be solved by changing the MTI interface or better tolerancing the slider mechanism. The most promising solution is to improve on the coupling interface requiring less or no force to engage and make it self centering. No issue has been found when the distal section is removed, the MTIs disengage properly without issues.

Distal MTIs

Ideally the distal MTIs are manufactured using FDM printing. However, the overhangs in the current design need supports or the part needs to be oriented horizontally to be printed. Both options gave unsatisfying results: Supports need to be removed and leave a rough finish requiring a lot of post processing to get the fit with other parts right. When the model is printed oriented horizontally, print artifacts alter the fit with other parts. Part of the model needs to be cut away for proper print bed adhesion, resulting in a non circular shape. Also due to the cylindrical shape of the model, when in horizontal orientation an overhang is formed which requires supports or otherwise sags. This leaves too many artifacts in the part. Therefore, this part was printed using SLA. The model was oriented horizontally in the slicer which gave a good result. Future work could try to come up with a better design that can be printed with FDM, however a different MTI system could improve connecting and disconnecting the section.

Connecting tendons to the MTIs can be done using knots in possibly in combination with glue for slippery tendons such as Dyneema. The disadvantage of this method is the semi permanent bond between the tendons and MTI, depending on the glue used. For a more reusable approach, the MTI should have a different design for the fixation of the tendons. A small clamping mechanism could be designed to firmly grab the tendons. This can be challenging though with small and slippery tendon materials. Also the tendon should not be damaged when it is clamped. This potentially causes the tendon to break under load.

5.2.4. MTI lock

The MTI lock worked well, the MTIs stay in place when the distal section is removed and it unlocks the MTIs correctly when the locking ring is actuated. Despite all the parts being FDM printed, in-

cluding the pivoting pins, the mechanism works as intended and little play was noticed during use. The assembly of this mechanism was fairly straightforward and the parts require little to no cleanup. In the locking ring the small printed membranes in the holes for the link need to be cut away and the tiny bridges and custom supports for the retention tabs in the ring also require cleanup.

5.2.5. Connector

The connector that couples the proximal and distal section keeps the parts tightly fixed together. A minor disadvantage is the symmetric design, allowing the distal section to be installed in two orientations. This can be simply resolved by adding external markers like arrows that indicate where the parts should align, often used for camera lenses. A more robust solution would be to also change the geometry of one of the tabs to physically allow only one orientation. The supports printed under the cantilevered parts in the proximal and distal connector need to be removed after printing, which is relatively easy when the support settings of the slicer are dialed in.

5.2.6. Force sensor

The goal was to make a force sensor that is low-cost. This was successful as the force sensor can be made for €2.11 a piece when the Hall sensors are bought in higher quantities, e.g. 25 or more. Even if only single quantities are bought, the price is still only €2.93. The magnets used cost €0.34 a piece and the material used for printing, considering a spool of PLA costing €20 per kg, is only €0.34. As mentioned in Section 5.1, this low cost comes with some disadvantages in terms of precision and accuracy, however with more research this force sensor has the potential to be improved to increase performance.

The requirement of 50 N has not been met as only 40 N was achieved with the proposed design. This is partly caused by the limited range of the Hall sensor that could be used due to the sub-optimal magnet size. On the other hand, the deflection caused by an applied force of 50 N causes plastic deformation as was found when testing the flexure design. Despite demonstrating a strong linear relationship between force and deflection, the linear beam theory was stretched beyond its original limits where only small deflections are assumed. With final maximal deflection of around 3.7 mm compared to a combined flexure length of 30mm. This gives a deflection of 12.3% of the flexure length. Note that the flexures on both the proximal and distal side of the force sensor are in series. Also the E modulus of the printed mate-

rial is not known with certainty and can vary within prints, filament brand and type. It was made sure to use the same printer, printer settings, printing material from the same spool for the fabrication of the force sensors.

Assembly wise it is fairly straightforward to put the sensor together. Only minor cleanup is needed after the print has finished, the small bridge connecting the distal and proximal section together needs to be cut away as well as the tiny bridge in the MTI to allow the locking pall to be pressed. The Hall effect sensor can be glued in place using cyanoacrylate and the magnet is pressed in the slot opposing the sensor. Placing the magnet correctly requires the user to monitor the ADC output of the micro-controller and adjust the magnet until the required value is read. This can be slightly tedious as the slightest movement of the magnet gives a relatively large change in sensor output. Once the magnet is at the desired location a dab of glue secures the magnet permanently. For a non permanent fixation, hot glue can be used which is fairly easy to remove by hand, enabling the user to reset the magnet if necessary.

5.2.7. Actuation unit

Actuator placement

The proposed design can house up to 12 actuators which could actuate manipulator with three segments. The design has the potential to be altered to house more actuators for manipulators with more segments. However a larger printer will be required to do manufacture the larger parts. Alternatively these parts, such as the plates and tendon diffuser, can be strategically cut in sections for printing and be assembled in to a complete part. Increasing the amount of actuators enlarges the hollow cavity of the design. This space can be used to house the electronics. For a large number of segments it may be useful to change the pattern in which the actuators are placed to avoid very large prints and use the space more efficiently. However, for such high number of actuators it may make sense to completely alter the actuation unit to use cheaper parts. A clever solution could be found to only use a minimum number of actuators, where each actuator can actuate multiple tendons of the manipulator. For example, utilise four actuators that can advance each segment sequentially. Though, this means that not all segments can be actuated simultaneously.

Linear guide

There is some play in the linear guide that causes clearance issues as described in Section 5.2.3. However, not only coupling is subjected to this

issue. Moving the actuators can cause the force sensor assembly to interfere with the plates through which it moves. Especially when there is no or not enough tension on the attached tendons. The sensor and distalMTI can get stuck on the plates. This issue can be resolved by making the slider bushing longer and improving the tolerance between the rods and slider bushing. Using off the shelf guide rods and bushings designed to be used together could also reduce or eliminate this problem.

5.2.8. Changing manipulators

Manipulators can be changed using the removable distal section. The distal MTIs can be manually placed into the MTI lock and locked into position. An upgrade would be to utilize a jig, into which the MTIs can be placed to align them with the MTI lock. This would be especially helpful when a manipulator has multiple segments.

5.2.9. Electronics

Force sensor resolution

The Arduino Mega 2560 rev.3 has a 10 bit ADC, meaning 1024 data points, resolution. A different microcontroller can be used to increase the resolution. With a maximum load of 40 N this gives a maximum theoretical resolution of 0.039 N. However the magnet and Hall sensor combination was not ideal and only 800 points could be used giving a resolution of 0.05 N. The S-shaped curve emerged from the current sensor and magnet combination for the required deflection of the spring gives unusable values at the lower and top end of the graph. These parts of the graph could potentially be used with a higher order fit and more calibration points. However, a better solution is to use a magnet that is longer, e.g. 8 or 10 mm instead of the 5 mm long magnet that is currently used.

There are two ways of improving the resolution. The most straightforward solution is to use a micro controller with a higher resolution ADC. On the other hand, optimizing the magnet and Hall sensor combination for a given deflection can give a more linear response, especially at lower and higher ADC values. Currently only 800 out of 1024 data points are used.

Distance measurement

The current design relies on the stepper motors not skipping steps and the micro controller correctly counting the steps send to the stepper motor. This can work adequately as this is currently done with most low and mid end FDM 3D printers. However, especially with higher forces, the motors

could potentially skip steps when the load or acceleration is too large. Also the distance of the tendons is inferred by converting the step count of the motors to mm and subtracting the extension of the sensor. This extension is converted from ADC values to mm using a third order data fit. There is an error dependency on pulling and releasing a load for this extension. Also, creep due to a constant applied load extends the force sensor over time. These errors make determining the precise actuated tendon length a non trivial task. Therefore when higher precision is important, an external sensors that keeps track of the traversed distance of only the tendons is advised. Off course, the downside of using extra sensor is the increased cost and complexity associated with them.

5.2.10. Test setup software

The program for the setup is written for manipulators with only one segment. However, the script can be adjusted to allow for more manipulators and different actuation sequences. These can include but are not limited to circular motion at varying bending radii, move to predefined coordinates, etc.

The program moves the antagonistic tendon the same amount as the pulling tendon, but in opposite direction. As demonstrated in Fig. 4.12b and Fig. 4.13b the force turns negative when the tendon is eased. It was visually observed that the easing tendons became slack, resulting in the elimination of the previously applied pretension. The program can be altered to always have pretension on the easing tendon. However this requires a PID controller to keep the pretension at the desired level, which need to be tuned.

5.2.11. Utility of the prototype

The prototype is not perfect, however it is capable of doing its intended purpose: Performing tests with tendon-driven instruments using Besides the practical issues as the MTI coupling and the loose slider fit, which can be overcome by spending some more time tuning the tolerances, the viscoelastic behaviour of PLA used as the spring is the biggest issue of the prototype. This essentially dictates the accuracy of the force sensor. Especially when subjected to loads for longer periods of time, the sensor could read higher forces than actually applied. Applying tension on the force sensor should be limited to relative short duration, max 1 minute, to limit the viscoelastic errors. Though, shorter exposure to high loads is preferable. After applying loads it is advised to let the sensors relax for a moment in the absence of load. Switch-

ing between manipulators is relatively straightforward. A jig could be used to conveniently attach the tendons of the manipulator to the distal MTI before it is placed in the distal section of the setup in stead of measuring the cable lengths. The use of a microcontroller allows for a highly adaptable test procedure that can be coded in C or C++. A test procedure can be programmed based on the test protocol of the user.

5.3. Requirements fulfillment

Two tendon driven manipulators, one with 8 mm and one with 20 mm outer diameter are successfully tested on the prototype. An Arduino microcontroller, stepper motor drivers and linear non-captive stepper motors are used to actuate the tendons. A detachable distal section is used to connect the manipulator in a non-permanent way to the setup which is fixed during use and can be removed by pressing two buttons simultaneously. The tendon displacement is determined by counting the number of steps taken by the stepper motors and multiplying this by the linear advancement per step. A custom designed force sensor based on a spring and a Hall effect sensor was used to determine the force in the tendons. The setup does not include a sensor for measuring the tendon displacement. However, the displacement can be determined by tracking the number of steps taken by the stepper motors and multiplying this number by the advancement per step of the lead screw. The force sensor can be calibrated by suspending known weights from it. The test program pretensions the tendons to 1 N, or 15 ADC points, before the test sequence takes place. The prototype is made open source and all the CAD and program files can be found on GitHub [52]. Only off the shelf components and custom designed parts that can be printed on a FDM printer are used. The bill of materials can be found in Table A.1 The actuation range is 100 mm with a theoretical resolution of 6.4 μm per step. The actual resolution however, due to the viscoelastic properties of the force sensor, is lower as an error up to 0.15 mm is introduced and thus not fulfilling the resolution requirement. In stead of the required 50 N, only up to 39.8 N was reached with the tension sensor. This was caused by the limited useable range of the magnet and Hall sensor combination. Preliminary investigation of the spring performance showed that the spring of the sensor was able to go up to 50 N. The tension sensors cost only €2.11 and the whole setup with 12 actuators would cost around €950. The prototype has a central hole that can potentially be used to

insert instruments into manipulators connected to the setup. However the feasibility was not further assessed. The final prototype, without a manipulator attached, fits in a box sized $l = 470$ mm, $w = 220$ mm, $h = 240$ mm. All the custom parts can be printed on a printer with a 220 mm x 220 mm x 250 mm volume.

5.4. Further study & recommendations

5.4.1. Sensor leaf spring

The force sensor is made of FDM printed PLA. This material is not ideal for flexible and compliant applications. The effects of creep and cyclic loading should be further investigated to get a better understanding of the sensor performance and behaviour. Alternatively other FDM printing materials can be investigated to be used as the print material. However, besides the limitations, the material has shown promising results. The question remains if the benefits of low-cost manufacturing and adjustable design outweigh the drawbacks of viscoelasticity and moderate resolution. The sensor is suitable for getting an indication of the performance of a manipulator. For more precision and better resolution, further research is required. The printed springs can be changed for spring steel which has no viscoelastic effects. However, in the current design this requires manual assembly which could be tedious. One could try printing the spring body and pressing heated spring steel leaves into the body for assembly. Using spring steel likely has an effect on Hall effect sensor reading due to the ferromagnetic property of spring steel. If the effect is understood it can be accounted for to get better results. For example, a well calibrated fit can be used to convert the output of the Hall sensor to Newton.

5.4.2. Sensor interference

In the current design only four sensors are used that are placed relatively far apart. If additional sensors are to be incorporated into the setup, it is crucial to understand the extend to which the magnetic fields of the magnets in the force sensors influence the Hall readings of neighbouring sensors. This effect was not investigated in this thesis. When sensors are affecting each other, weaker magnets could be implemented for a reduction of the effect. Different Hall sensors are then likely to be required to get the linear relation between displacement and sensor output.

5.4.3. Interaction magnet and Hall sensor

More research can be done to improve the linear response of the sensor. The interaction between the magnet and Hall effect sensor should be better understood. FEM analysis on the magnetic field of magnets could be performed to find better suited magnets for the Hall sensor and motion range. The useable range of the sensor was limited due to the size of the magnet used in this thesis. A longer magnet probably yields a better linear response in the actuation range of the spring as the linear magnetic gradient range is extended over a longer distance.

5.4.4. Manipulator angle measurement

Measuring the angle of the manipulator during testing falls outside the scope of this thesis. However, it is an important property that is required to fully characterize a manipulator. Multiple methods exist to measure this angle. It depends on the specific requirements of the user which method is best to use. Cameras, optical trackers, FBG and electromagnetic tracking are examples that could be implemented. Each have their advantages and disadvantages. Camera's and optical trackers can only be used to characterise the performance of the instrument outside any opaque substance or tissue. Optical trackers require additional physical markers added on the manipulator. FBG requires a glass fiber to be installed inside the manipulator. However it has the benefit of being able to be used in tissue or other materials normally occluding direct visual contact when using a camera. The magnetic sensors also require extra hardware to be installed into the manipulator in the form of spools. Also external equipment is required to generate a magnetic field. The advantage however is that like with FBG the manipulator can be tested for example inside tissue and assess its properties in a surgical setting.

6

Conclusion

In this work a open source prototype test setup for tendon-driven manipulators with low cost, €2.11, custom built force sensors has been designed and tested. The whole design can be build using off the shelf and 3D printed parts. Manipulators with a diameter of up to 20 mm can be tested using the proposed setup. The modularity of the design allows compatibility for manipulator with multiple segments. A custom built low cost 3d printed force sensor using a magnet, Hall effect sensor and flexures was designed to measure the tendon tension of a manipulator while it is being actuated. Although requiring some improvements and further research, the concept of this sensor is promising especially if very high precision is not required. The build sensor has maximum deviation of ± 1.4 N and a 0-40 N range. Different manipulators can be switched out with little effort using the removable distal section of the setup. Despite some issues with loose tolerances, the setup works as intended and with the right upgrades and improvements these issues can be eliminated. Two manipulator designs were tested to showcase the capability of the setup. The design can be used to further explore manipulator designs for various medical applications and allows for comparing different designs and design iterations.

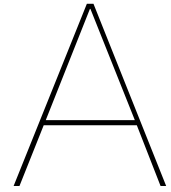
Bibliography

- [1] Zichen Zhao and Jin Gu. "Open surgery in the era of minimally invasive surgery". In: *Chinese Journal of Cancer Research* 34.1 (2022), p. 63. DOI: 10.1002/14651858.cd001546.pub4. URL: <https://doi.org/10.1002/14651858.cd001546.pub4>.
- [2] Thomas Jaschinski et al. "Laparoscopic versus open surgery for suspected appendicitis". In: *Cochrane Database of Systematic Reviews* 2018.11 (Nov. 2018). DOI: 10.1002/14651858.cd001546.pub4. URL: <https://doi.org/10.1002/14651858.cd001546.pub4>.
- [3] Andrew Lekarczyk et al. "Complications in Cervical and Thoracic Spine Surgery". In: *Journal of Minimally Invasive Spine Surgery and Technique* 8.1 (Apr. 2023), pp. 97–104. DOI: 10.21182/jmisst.2023.00654. URL: <https://doi.org/10.21182/jmisst.2023.00654>.
- [4] Josefin Petersson et al. "Short term results in a population based study indicate advantage for laparoscopic colon cancer surgery versus open". In: *Scientific Reports* 13.1 (Mar. 2023). DOI: 10.1038/s41598-023-30448-8. URL: <https://doi.org/10.1038/s41598-023-30448-8>.
- [5] Stefano Uccella et al. "Laparoscopic vs. open treatment of endometrial cancer in the elderly and very elderly: An age-stratified multicenter study on 1606 women". In: *Gynecologic Oncology* 141.2 (May 2016), pp. 211–217. DOI: 10.1016/j.ygyno.2016.02.029. URL: <https://doi.org/10.1016/j.ygyno.2016.02.029>.
- [6] Michael Y. Wang et al. "Acute Hospital Costs After Minimally Invasive Versus Open Lumbar Interbody Fusion". In: *Journal of Spinal Disorders & Techniques* 25.6 (Aug. 2012), pp. 324–328. DOI: 10.1097/bsd.0b013e318220be32. URL: <https://doi.org/10.1097/bsd.0b013e318220be32>.
- [7] Andreas Meinzer et al. "Advances and Trends in Pediatric Minimally Invasive Surgery". In: *Journal of Clinical Medicine* 9.12 (Dec. 2020), p. 3999. ISSN: 2077-0383. DOI: 10.3390/jcm9123999. URL: <http://dx.doi.org/10.3390/jcm9123999>.
- [8] J. Amat et al. "Challenges in the Design of Laparoscopic Tools". In: *Advances in Intelligent Systems and Computing*. Springer International Publishing, Nov. 2015, pp. 463–475. DOI: 10.1007/978-3-319-27149-1_36. URL: https://doi.org/10.1007/978-3-319-27149-1_36.
- [9] Filip Jelínek et al. "Classification of Joints Used in Steerable Instruments for Minimally Invasive Surgery—A Review of the State of the Art". In: *Journal of Medical Devices* 9.1 (Mar. 2015). DOI: 10.1115/1.4028649. URL: <https://doi.org/10.1115/1.4028649>.
- [10] Takayuki Asao, Hiroyuki Kuwano, and Erito Mochiki. "Laparoscopic surgery update for gastrointestinal malignancy". In: *Journal of Gastroenterology* 39.4 (Apr. 2004), pp. 309–318. DOI: 10.1007/s00535-004-1331-z. URL: <https://doi.org/10.1007/s00535-004-1331-z>.
- [11] Irene Rivas-Blanco et al. "Transferring Know-How for an Autonomous Camera Robotic Assistant". In: *Electronics* 8.2 (Feb. 2019), p. 224. ISSN: 2079-9292. DOI: 10.3390/electronics8020224. URL: <http://dx.doi.org/10.3390/electronics8020224>.
- [12] CC BY 4.0 Deed | Attribution 4.0 International | Creative Commons — creativecommons.org/licenses/by/4.0/. [Accessed 02-04-2024].
- [13] Christine Deguara and Colin Davis. "Laparoscopic entry techniques". In: *Current Opinion in Obstetrics & Gynecology* 23.4 (Aug. 2011), pp. 268–272. DOI: 10.1097/gco.0b013e328348bd61. URL: <https://doi.org/10.1097/gco.0b013e328348bd61>.
- [14] John R. Romanelli and David B. Earle. "Single-port laparoscopic surgery: an overview". In: *Surgical Endoscopy* 23.7 (Apr. 2009), pp. 1419–1427. DOI: 10.1007/s00464-009-0463-x. URL: <https://doi.org/10.1007/s00464-009-0463-x>.

- [15] Kunyong Lyu, Lixiao Yang, and Chengli Song. "Motion Measurement and Analysis of Different Instruments for Single-Incision Laparoscopic Surgery". In: *Applied Bionics and Biomechanics 2022* (June 2022). Ed. by Fahd Abd Algalil, pp. 1–8. DOI: 10.1155/2022/3057485. URL: <https://doi.org/10.1155/2022/3057485>.
- [16] Costanza Culmone et al. "Comparison of two cable configurations in 3D printed steerable instruments for minimally invasive surgery". In: *PLOS ONE* 17.10 (Oct. 2022). Ed. by Antonio Riveiro Rodríguez, e0275535. DOI: 10.1371/journal.pone.0275535. URL: <https://doi.org/10.1371/journal.pone.0275535>.
- [17] Victor F. Muñoz et al. "On laparoscopic robot design and validation". In: *Integrated Computer-Aided Engineering* 10.3 (June 2003), pp. 211–229. DOI: 10.3233/ica-2003-10301. URL: <https://doi.org/10.3233/ica-2003-10301>.
- [18] Won-ho Shin, Seong-young Ko, and Dong-soo Kwon. "Design of a Dexterous and Compact Laparoscopic Assistant Robot". In: *2006 SICE-ICASE International Joint Conference*. IEEE, 2006. DOI: 10.1109/sice.2006.315613. URL: <https://doi.org/10.1109/sice.2006.315613>.
- [19] Hyunsuk Frank Roh, Seung Hyuk Nam, and Jung Mogg Kim. "Robot-assisted laparoscopic surgery versus conventional laparoscopic surgery in randomized controlled trials: A systematic review and meta-analysis". In: *PLOS ONE* 13.1 (Jan. 2018). Ed. by Ganesh Dangal, e0191628. DOI: 10.1371/journal.pone.0191628. URL: <https://doi.org/10.1371/journal.pone.0191628>.
- [20] Renfeng Xue et al. "Design and Evaluation of FBG-Based Tension Sensor in Laparoscope Surgical Robots". In: *Sensors* 18.7 (June 2018), p. 2067. DOI: 10.3390/s18072067. URL: <https://doi.org/10.3390/s18072067>.
- [21] Huu Minh Le, Thanh Nho Do, and Soo Jay Phee. "A survey on actuators-driven surgical robots". In: *Sensors and Actuators A: Physical* 247 (Aug. 2016), pp. 323–354. DOI: 10.1016/j.sna.2016.06.010. URL: <https://doi.org/10.1016/j.sna.2016.06.010>.
- [22] P Breedveld et al. "A new, easily miniaturized steerable endoscope". In: *IEEE Eng. Med. Biol. Mag.* 24.6 (Nov. 2005), pp. 40–47.
- [23] Russell H. Taylor et al. "Medical Robotics and Computer-Integrated Surgery". In: *Springer Handbook of Robotics*. Springer International Publishing, 2016, pp. 1657–1684. DOI: 10.1007/978-3-319-32552-1_63. URL: https://doi.org/10.1007/978-3-319-32552-1_63.
- [24] Arturo Marbán et al. "Haptic Feedback in Surgical Robotics: Still a Challenge". In: *Advances in Intelligent Systems and Computing*. Springer International Publishing, 2014, pp. 245–253. ISBN: 9783319034133. DOI: 10.1007/978-3-319-03413-3_18. URL: http://dx.doi.org/10.1007/978-3-319-03413-3_18.
- [25] Przemyslaw Korzeniowski et al. "NOViSE: a virtual natural orifice transluminal endoscopic surgery simulator". In: *International Journal of Computer Assisted Radiology and Surgery* 11.12 (June 2016), pp. 2303–2315. ISSN: 1861-6429. DOI: 10.1007/s11548-016-1401-8. URL: <http://dx.doi.org/10.1007/s11548-016-1401-8>.
- [26] Jacques Marescaux. "Surgery Without Scars: Report of Transluminal Cholecystectomy in a Human Being". In: *Archives of Surgery* 142.9 (Sept. 2007), p. 823. ISSN: 0004-0010. DOI: 10.1001/archsurg.142.9.823. URL: <http://dx.doi.org/10.1001/archsurg.142.9.823>.
- [27] Michael F. McGee et al. "A Primer on Natural Orifice Transluminal Endoscopic Surgery: Building a New Paradigm". In: *Surgical Innovation* 13.2 (June 2006), pp. 86–93. ISSN: 1553-3514. DOI: 10.1177/1553350606290529. URL: <http://dx.doi.org/10.1177/1553350606290529>.
- [28] Ibrahim A. Seleem, Haitham El-Hussieny, and Hiroyuki Ishii. "Recent Developments of Actuation Mechanisms for Continuum Robots: A Review". In: *International Journal of Control, Automation and Systems* 21.5 (May 2023), pp. 1592–1609. DOI: 10.1007/s12555-022-0159-8. URL: <https://doi.org/10.1007/s12555-022-0159-8>.

- [29] Theodosia Lourdes Thomas. “Bending the rules: Magnetically-actuated surgical continuum manipulators”. PhD thesis. DOI: 10.3990/1.9789036555913. URL: <https://doi.org/10.3990/1.9789036555913>.
- [30] Costanza Culmone et al. “Follow-The-Leader Mechanisms in Medical Devices: A Review on Scientific and Patent Literature”. In: *IEEE Reviews in Biomedical Engineering* 16 (2023), pp. 439–455. DOI: 10.1109/rbme.2021.3113395. URL: <https://doi.org/10.1109/rbme.2021.3113395>.
- [31] Jessica Burgner-Kahrs. *Tendon-driven Continuum Robots — opencontinuumrobotics.com*. <https://www.opencontinuumrobotics.com/101/2022/11/11/tdcr-intro.html>. [Accessed 17-04-2024].
- [32] Xiangyu Luo et al. “A Novel Distal Hybrid Pneumatic/Cable-Driven Continuum Joint with Variable Stiffness Capacity for Flexible Gastrointestinal Endoscopy”. In: *Advanced Intelligent Systems* 5.6 (Mar. 2023). ISSN: 2640-4567. DOI: 10.1002/aisy.202200403. URL: <http://dx.doi.org/10.1002/aisy.202200403>.
- [33] Botao Lin et al. “A Modular Lockable Mechanism for Tendon-Driven Robots: Design, Modeling and Characterization”. In: *IEEE Robotics and Automation Letters* 7.2 (Apr. 2022), pp. 2023–2030. ISSN: 2377-3774. DOI: 10.1109/lra.2022.3142907. URL: <http://dx.doi.org/10.1109/LRA.2022.3142907>.
- [34] Xiaoyong Wei et al. “Design and analysis of a continuum robot for transnasal skull base surgery”. In: *The International Journal of Medical Robotics and Computer Assisted Surgery* 17.6 (Sept. 2021). ISSN: 1478-596X. DOI: 10.1002/rcs.2328. URL: <http://dx.doi.org/10.1002/rcs.2328>.
- [35] Wenjun Xu, Deren Meng, and Hongliang Ren. “Comparative mechanical analysis for flexible bending manipulators with quad-tendon antagonistic pairs”. In: *Flexible Robotics in Medicine*. Elsevier, 2020, pp. 249–267. DOI: 10.1016/b978-0-12-817595-8.00011-0. URL: <http://dx.doi.org/10.1016/B978-0-12-817595-8.00011-0>.
- [36] Fei Qi et al. “Kinematics optimization and static analysis of a modular continuum robot used for minimally invasive surgery”. In: *Proceedings of the Institution of Mechanical Engineers, Part H: Journal of Engineering in Medicine* 232.2 (Dec. 2017), pp. 135–148. ISSN: 2041-3033. DOI: 10.1177/0954411917747008. URL: <http://dx.doi.org/10.1177/0954411917747008>.
- [37] Manuela Eugster et al. “Robotic Endoscope System for Future Application in Minimally Invasive Laser Osteotomy: First Concept Evaluation”. In: *IEEE Transactions on Medical Robotics and Bionics* 4.3 (Aug. 2022), pp. 621–633. ISSN: 2576-3202. DOI: 10.1109/tmr.2022.3172471. URL: <http://dx.doi.org/10.1109/TMRB.2022.3172471>.
- [38] Xiaoyong Wei et al. “Modeling and control of cable-driven continuum robot used for minimally invasive surgery”. In: *Proceedings of the Institution of Mechanical Engineers, Part H: Journal of Engineering in Medicine* 237.1 (Dec. 2022), pp. 35–48. ISSN: 2041-3033. DOI: 10.1177/09544119221135664. URL: <http://dx.doi.org/10.1177/09544119221135664>.
- [39] Jie Wang et al. “A Novel Miniature Spring-Based Continuum Manipulator for Minimally Invasive Surgery: Design and Evaluation”. In: *IEEE/ASME Transactions on Mechatronics* 28.5 (Oct. 2023), pp. 2716–2727. ISSN: 1941-014X. DOI: 10.1109/tmech.2023.3252279. URL: <http://dx.doi.org/10.1109/TMECH.2023.3252279>.
- [40] Yixuan Kong et al. “Design and Kinematic Modeling of In-Situ Torsionally-Steerable Flexible Surgical Robots”. In: *IEEE Robotics and Automation Letters* 7.2 (Apr. 2022), pp. 1864–1871. ISSN: 2377-3774. DOI: 10.1109/lra.2022.3142920. URL: <http://dx.doi.org/10.1109/LRA.2022.3142920>.
- [41] Fei Qi et al. “Dynamic model and control for a cable-driven continuum manipulator used for minimally invasive surgery”. In: *The International Journal of Medical Robotics and Computer Assisted Surgery* 17.3 (Mar. 2021). ISSN: 1478-596X. DOI: 10.1002/rcs.2234. URL: <http://dx.doi.org/10.1002/rcs.2234>.

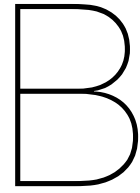
- [42] <https://www.dmws.nl/>. *FUTEK LSB205 Miniature S-Beam Jr. Load Cell 2.0* — *pimzos.com*. <https://www.pimzos.com/en/lsb205.html>. [Accessed 03-11-2023].
- [43] K. van den Berg. "Patent Review of Mechanical Connectors in Medical Instruments". 2022.
- [44] *123-3D.nl - 3D-printers | kits | parts | filament* — *123-3d.nl*. <https://www.123-3d.nl/3D-printers/Alle-3D-printers-p43459.html?519=1i925>. [Accessed 13-02-2024].
- [45] *Beam theory: Bending - JPE* — *jpe-innovations.com*. <https://www.jpe-innovations.com/precision-point/beam-theory-bending/>. [Accessed 25-01-2024].
- [46] Wang et al. "Effect of Porosity on Mechanical Properties of 3D Printed Polymers: Experiments and Micromechanical Modeling Based on X-Ray Computed Tomography Analysis". In: *Polymers* 11.7 (July 2019), p. 1154. ISSN: 2073-4360. DOI: 10.3390/polym11071154. URL: <http://dx.doi.org/10.3390/polym11071154>.
- [47] Tom Stanton. *How I Designed a 3D Printed Wing* — *youtube.com*. https://www.youtube.com/watch?v=QJjhMan6T_E. [Accessed 27-01-2024].
- [48] *Hall Effect Position Sensing: Response Linearity and Slope for Slide-By Configurations - Technical Articles* — *allaboutcircuits.com*. <https://www.allaboutcircuits.com/technical-articles/hall-effect-position-sensing-response-linearity-and-slope-for-slide-by-configurations/>. [Accessed 26-01-2024].
- [49] *NEMA 11 Non-Captive Acme Linear Stepper Motor 1.0A 32.2mm Stack Screw Lead 1.27mm(0.05" Lead Length 200mm - 11N13S1004FD5-200RS|STEPPERONLINE* — *omc-stepperonline.com*. <https://www.omc-stepperonline.com/nema-11-non-captive-acme-linear-stepper-motor-1-0a-32-2mm-stack-screw-lead-1-27mm-0-05-lead-length-200mm-11n13s1004fd5-200rs>. [Accessed 22-01-2024].
- [50] *Demo of Prototype* — *youtu.be*. <https://youtu.be/gquCTrKaKgA>. [Accessed 05-05-2024].
- [51] <https://data.4tu.nl/>. [Accessed 05-05-2024].
- [52] Kees van den Berg. *GitHub - KeesvdBerg/TDM-Test-Setup: Test setup for tendon-driven manipulators* — *github.com*. <https://github.com/KeesvdBerg/TDM-Test-Setup>. [Accessed 05-05-2024].
- [53] Fabian Trauzettel et al. *3Flex - 3D Printable Parametric Tendon-driven Manipulator*. 2023. DOI: 10.4121/21666116. URL: https://data.4tu.nl/articles/_/21666116.
- [54] Costanza Culmone et al. "Exploring non-assembly 3D printing for novel compliant surgical devices". In: *PLOS ONE* 15.5 (May 2020). Ed. by Tommaso Ranzani, e0232952. ISSN: 1932-6203. DOI: 10.1371/journal.pone.0232952. URL: <http://dx.doi.org/10.1371/journal.pone.0232952>.
- [55] *DRV5055 Ratiometric Linear Hall Effect Sensor Data Sheet*. [Accessed 16-03-2024]. Texas Instruments, Inc. Dallas, Texas, USA.



Bill of Materials

Table A.1: Bill of materials for a fully equipped test setup for manipulators containing 3 segments

| ITEM NO. | PART NAME | QTY. |
|----------|---|------|
| 1 | Motor mounting plate | 1 |
| 2 | Proximal section alignment plate | 1 |
| 3 | Proximal connector ring | 1 |
| 4 | Distal connector ring | 1 |
| 5 | MTI lock actuation ring | 1 |
| 6 | MTI lock mounting plate | 1 |
| 7 | Tendon diffuser | 1 |
| 8 | Instrument adapter | 1 |
| 9 | Guiding rod 3 mm | 24 |
| 10 | Hall sensor DRV5505 | 12 |
| 11 | Nema 11 non-captive stepper motor | 12 |
| 12 | Slider cap | 12 |
| 13 | Limit switch board | 12 |
| 14 | M2.5 bolt 10mm | 48 |
| 15 | M2.5 washer | 48 |
| 16 | M3 bolt 10 mm | 36 |
| 17 | M3 locknut | 12 |
| 18 | M3 nut | 24 |
| 19 | M3 washer | 24 |
| 20 | M4 threaded rod 140 mm | 12 |
| 21 | M4 nut | 120 |
| 22 | M4 washer | 96 |
| 23 | Table stand | 2 |
| 24 | Magnet 5mm-5mm | 12 |
| 25 | Force sensor body | 12 |
| 26 | Cable clip for endstop | 12 |
| 27 | MTI Lock spacer | 12 |
| 28 | MTI Lock link | 12 |
| 29 | MTI Lock tab | 12 |
| 30 | Tendon MTI | 12 |
| 31 | M4 threaded rod 130 mm | 12 |
| 32 | Din 466 knob for m4 nut | 12 |
| 33 | MTI lock pivot pin | 12 |
| 34 | M4 eye hook | 12 |
| 35 | M3 heat set insert | 12 |
| 36 | Arduino Mega 2560 Rev3 | 1 |
| 37 | A4988 stepper driver | 12 |
| 38 | 24 V DC Mean Well NDR-120-24 power supply | 1 |
| 39 | Breadboard and wires | X |



Test Setup Manual

B.1. Assembly of the setup

To assemble the prototype the following methods can be used. This is considering all parts to be printed and ready to be assembled. The motors are mounted on the motor mounting plate using 10 mm m2.5 bolts and washers. Insert the m3 heat inserts into the force sensors using for example a soldering iron. Make sure the heat inserts are pressed in straight. It is best to assembly the magnet and hall sensors on the force sensor before putting them into the test setup. Make sure to check the polarity of the magnet before inserting it into the sensor. Then use a microcontroller to position the magnet until the desired output value is reached for the non-extended sensor. The sliders can then pressed into the force sensors, make sure they are fully inserted. A hammer can be used to carefully tap on the sliders. Place the sliders into the bushings on the motor mounting plate, check the orientation of the force sensors using the Solidworks assembly. Screw the spindle into the heat inserts in the force sensor, a dap of loctite can be used to make a secure connection. The slider caps can now be placed at the end of the actuation units usign a 10mm m3 bolt and locknut. The cable clip can be glued in place on the slider cap. The limit switch boards can be mounted onto the motor mouting plate using 10 mm m3 bolts washers and nuts. Check the model for the order of these parts, the washer goes between the board and the motor mounting plate.

Now take the proximal connector ring and carefully tread the 140mm threaded rods straight into the holes. Make sure that the threads are butted but not exceeding out of the ring. Note that it may be convenient to already put the proximal section alignment plate, nuts and washers into place, this saves the user some effort when the rods are already installed. Though this may be awkward to thread the rods into the connector ring. Put the proximal section alignment plate into place, and tighten the m4 nuts. On open ends of the rods, place two nuts and a washer, make sure to leave some 10 mm thread open to put the motor mounting plate into position. Check the distance between the proximal section alignment plate and the motor mounting plate to be 112.5 mm and tighten the double nuts. Use a washer and nut on each rod to fix the motor mounting plate into place. The proximal section is now finished.

For the distal section start of with the MTI lock mounting plate and install the MTI lock pivot pins in the corresponding holes. Press the MTI lock tabs into place on the pins. Put the MTI lock actuation ring into place and use the MTI lock links to connect the MTI lock tabs with the MTI lock actuation ring. Now thread the 130 mm m4 threaded rods into the distal connector ring, similar to the proximal connector. Add the MTI lock spacers to the threaded rods. Place the MTI lock mouting plate in position and use m4 washers and nuts to fix the parts together.

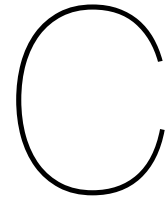
Proceed with adding the m4 eye hooks to the diffuser using m4 washers and nuts. First put on a m4 nut and washer on the eye bolt, put it into the diffuser and use a washer and nut to fix it in place. Make sure the distance between the spoke and eye hook is correct. This ensures proper allignement with the actuation units and force sensor. On the threaded rods, add double nuts and a washer, leaving space to put on the diffuser and make sure the distance between the MTI lock mounting plate and the diffucer is 75 mm Tighten the nuts. Install m4 nuts into the Din 466 knobs, place a washer on the threaded rods and tighten the knobs. The distal section is now finished.

The electronics can be installed on a breadboard using the schematic provided in Section 3.3.1. This schematic is only for 4 actuators, but can easily be expanded to 12 or more.

B.2. Using the setup

When all the parts are assembled the test setup is ready to be used. Make sure that the electronics are wired properly and check the polarity of the stepper motors. First the tendon MTI's need to be attached to the tendons. Assuming the tendons are already installed on the manipulator, one proceeds with threading the tendons through the customized manipulator adapter. The distance between the bottom of the adapter, as it is made in the CAD files, to the top of the MTI is 166 mm. Make sure to have the small groove on the MTI facing away from the manipulator when attaching the tendons. The manipulator and adaptor can now be placed into the distal section of the setup. Make sure that the MTI locking mechanism is in the open position. Place a tube over the manipulator to make sure that the manipulator is kept straight. Use the positioning jig to properly place the MTI's, again pay attention to face the groove away from the manipulator. Close the MTI lock when all MTI's are positioned correctly. The setup is now ready to be used.

Enable power of the setup. Upload the Arduino test script to the microcontroller. Open the matlab script on the computer and run it. Fill in the values of the manipulator radial tendon offset and the desired angular deflection. The setup homes the motors and moves to the installing position. Wait for the homing sequence to finish, a prompt will tell the user to install the distal section. Confirm correct installation. The system will now pretension the tendons. When the pretension sequence is finished, a popup tells the user to remove the tube from the manipulator. Confirm that the tube is removed and that the test can start. Wait for the test sequence to finish while making sure the setup does not get stuck or misbehaves. The sequence ends by moving to the installing position. The distal section can now be detached and the manipulator can be removed from the distal section.



Additional Graphs

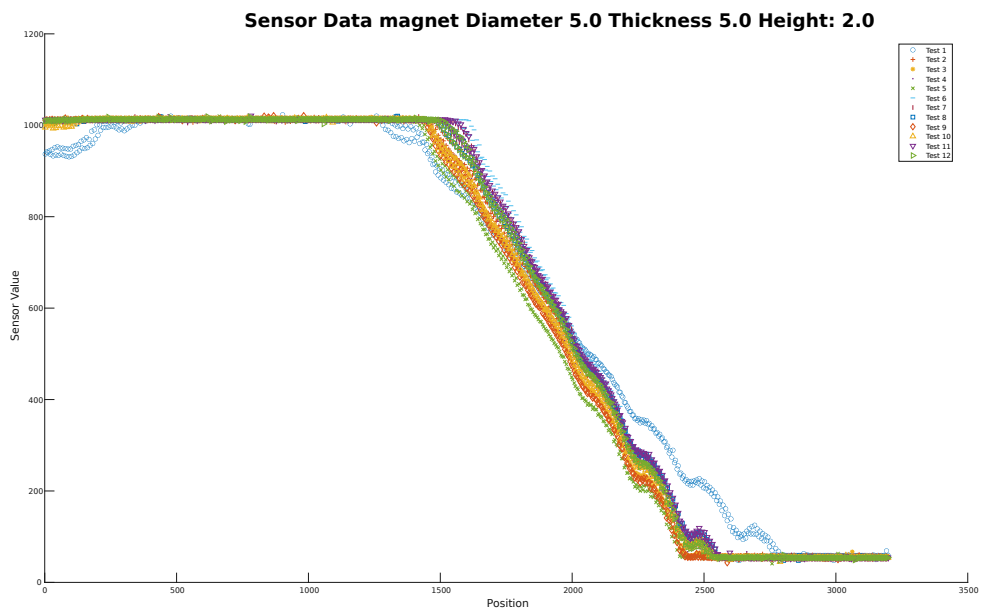


Figure C.1: Graphs of 12 magnets. Each magnets polarity was checked beforehand. The variation between the magnets is clearly visible. The dimensions are given in mm.

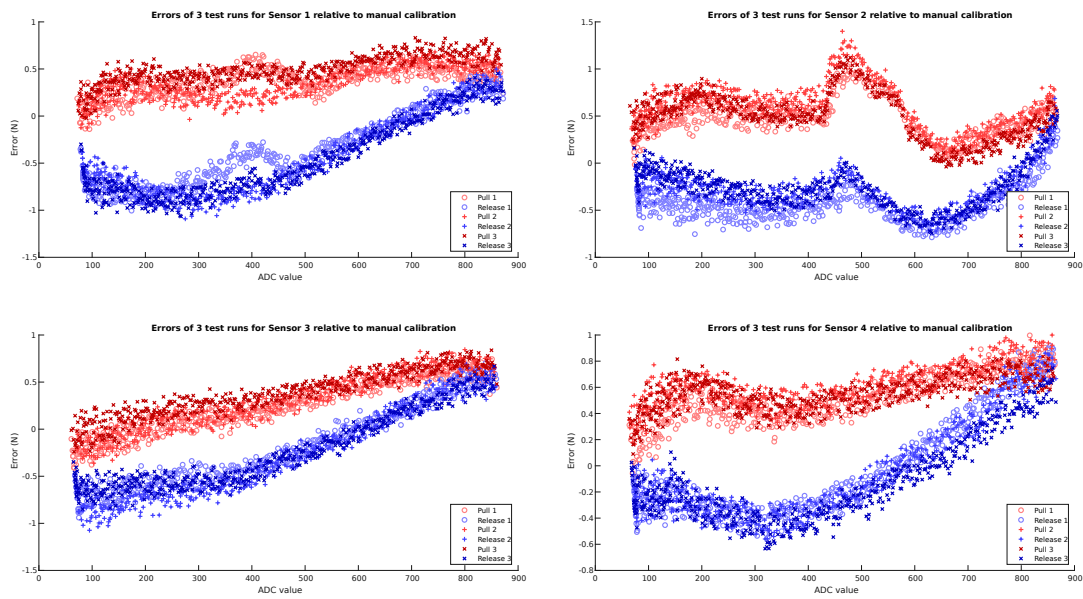


Figure C.2: The error between the measured data from the Futek load cell and the fitted calibration data. Each sensor is displayed where red is pulling and blue is releasing. The different shades and markers indicate the different tests.

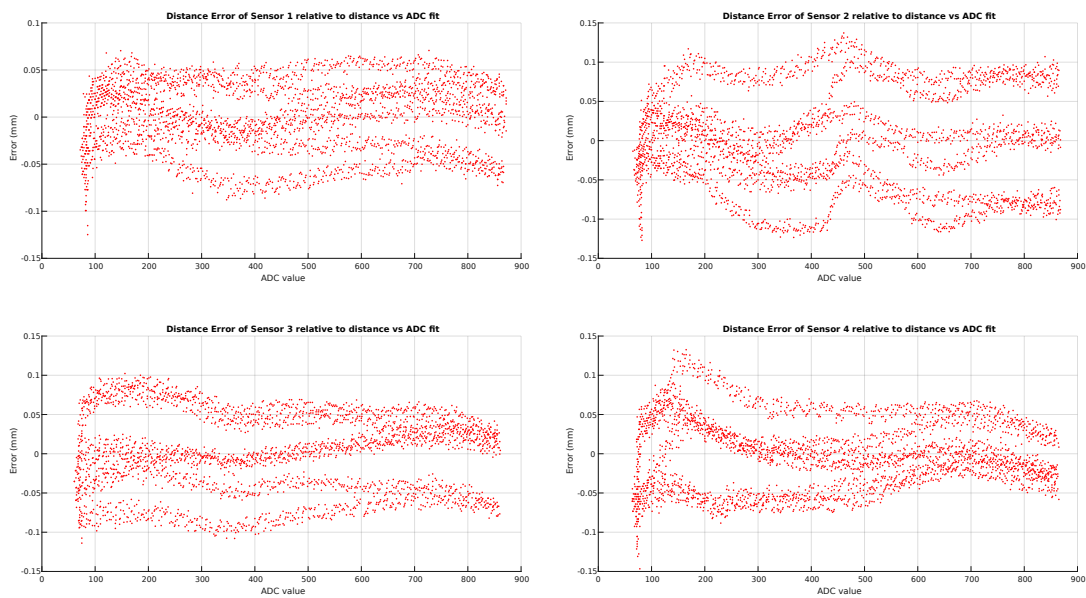


Figure C.3: The errors in extension between the fitted ADC values and the distance counted on the microcontroller in mm as a function of the ADC values or each sensor.